Monitoring land subsidence and its induced geological hazard with Synthetic Aperture Radar Interferometry: A case study in Morelia, Mexico

Francesca Cigna [a,*], Batuhan Osmanoğlu [a,1], Enrique Cabral-Cano [b], Timothy H. Dixon [a,2], Jorge Alejandro Ávila-Olivera [c], Víctor Hugo Garduño-Monroy [d], Charles DeMets [e], Shimon Wdowinski [a]

[a] Division of Marine Geology and Geophysics, University of Miami, 4600 Rickenbacker Causeway, Miami, FL 33149-1098, United States
[b] Departamento de Geomagnetismo y Exploración, Instituto de Geofísica, Universidad Nacional Autónoma de México, Ciudad Universitaria, 04510 México D.F., Mexico
[c] Instituto de Investigaciones Sobre los Recursos Naturales, Universidad Michoacana de San Nicolás de Hidalgo, Av. San Juanito Itzícuaro s/n, 58330, Morelia, Michoacán, Mexico
[d] Instituto de Investigaciones Metalúrgicas, Universidad Michoacana de San Nicolás de Hidalgo, Ciudad Universitaria, Edif. U, 58030 Morelia, Michoacán, Mexico
[e] Department of Geoscience, University of Wisconsin-Madison, 1215 Dayton, Madison, Wisconsin 53706, United States

ABSTRACT

Twenty three ENVISAT Synthetic Aperture Radar (SAR) images acquired in 2003–2010 were processed with conventional SAR Interferometry (InSAR) and Persistent Scatterer Interferometry techniques, to investigate spatial and temporal patterns of land subsidence in Morelia, Mexico. Subsiding areas are distributed as either concentrated circular patterns corresponding to intense groundwater extraction (e.g., Rio Grande meander area; maximum deformation of 7–8 cm/yr) or as elongate patterns oriented along NE–SW or E–W directions and parallel to major faults (i.e. La Colina, La Paloma and Central Camionera; maximum deformation of 4–5 cm/yr). High subsidence rates are also measured on the hanging wall of major normal faults, where the thickest sequences of compressible Quaternary sediments crop out. Strong contrasts in subsidence rates are identified across major faults, suggesting that these faults act as barriers to horizontal movement of groundwater. Subsidence rates show a weak positive correlation with the total thickness of compressible deposits, while there is no correlation with either water extraction rates or changes in static water level. Time-lapse analysis of ground deformation with conventional InSAR reveals temporal variations of subsidence north of the La Colina fault and the Rio Grande meander area. For this latter area, cross sections and 3D perspectives of InSAR measures, and analysis of subsidence rates through time, show an acceleration of subsidence velocities since 2005, corresponding to recasing of the Prados Verdes II well, whose location is centered in the area of highest subsidence.

© 2011 Elsevier Inc. All rights reserved.

1. Introduction

Many urban areas in Mexico derive all or part of their fresh water from local aquifers. Some of these cities have experienced significant population growth in the last few decades, and/or declining rainfall and reduced aquifer recharge. Without careful management, this can result in over-exploitation of the groundwater resource, leading to declining groundwater levels, compaction and loss of porosity in the aquifer, and surface subsidence. If over-exploitation is continued for too long, porosity losses become irreversible and aquifer capacity is permanently reduced. In these cases subsidence can also reach a few meters, enough to cause significant damage to urban infrastructure.

Monitoring surface movements associated with groundwater changes can be accomplished with Synthetic Aperture Radar (SAR) observations acquired by low Earth orbiting satellites. Since conventional SAR Interferometry (InSAR) was first applied in the early 1990s (Massonnet & Feigl, 1998; Rosen et al., 2000), it has been increasingly recognized as a valuable tool for groundwater-related problems, in both the single-interferogram (conventional) and the multi-interferogram (advanced) approaches (e.g., Amelung et al., 1999; Cabral-Cano et al., 2008; Galloway et al., 1998; Herrera et al., 2009; Hoffmann et al., 2001; Osmanoglu et al., 2011; Tomás et al., 2005). One of the challenges in applying the technique is that the observed surface deformation field may be complex, reflecting both tectonic and groundwater-related sources (e.g., Bawden et al., 2001). Multiple groundwater extraction locations, temporally and spatially variable extraction rates, and spatially variable mechanical properties

* Corresponding author at: Department of Earth Sciences, University of Firenze, Via La Pira 4, 50121 Firenze, Italy. Tel.: +1 305 421 4660, +39 055 2055300; fax: +1 305 421 4632, +39 055 2055317.
E-mail addresses: francesca.cigna@unifi.it, francesca.cigna@gmail.com (F. Cigna), bosmanoglu@alaska.edu (B. Osmanoğlu), ecabral@geofisica.unam.mx (E. Cabral-Cano), thd@usf.edu (T.H. Dixon), ja.avilaolivera@gmail.com (J.A. Ávila-Olivera), vgmonroy@umich.mx (V.H. Garduño-Monroy), chuck@geology.wisc.edu (C. DeMets), swdowinski@rsmas.miami.edu (S. Wdowinski).
[1] Present address: Geophysical Institute, University of Alaska, 903 Koyukuk Dr., Fairbanks, Alaska 99775-7320, United States.
[2] Present address: Department of Geology, University of South Florida, 4202 E. Fowler Avenue, SCA 528, Tampa, FL 33620–8100, United States.

and consequent variable responses to extraction may further complicate the interpretation.

Since the early 1980s the city of Morelia in Central Mexico has experienced subsidence associated with groundwater extraction in excess of natural recharge from rainfall. The surface deformation field reflects both tectonic and groundwater influences (e.g., Garduño-Monroy et al., 2001). In this paper, we present satellite SAR data for the period 2003–2010, and show that a time series analysis of these data is able to unravel most of the complexity. Specifically, we show that most of the variance of the subsidence signal can be explained by the location of major wells, the thickness of the underlying Quaternary sedimentary fill (the main aquifer) that overlies a faulted Miocene basement, and proximity to major faults. While some specific regions in the city show rapid subsidence and in some cases recently developed subsidence features, a larger part of the city does not yet exhibit extreme subsidence rates, suggesting that improved water resource management has the potential to greatly reduce or eliminate long term subsidence.

2. Geological and historical background

Morelia is the capital of the state of Michoacán in central Mexico. The original city center was built in the 16th century and is now a UNESCO World Heritage site. Beginning in the 1980s, Morelia experienced differential land subsidence, causing faulting and damage to urban infrastructure. Subsidence is commonly induced by consolidation of clay-rich lacustrine and fluvio-lacustrine sediments in response to over-exploitation of groundwater (e.g., Ávila-Olivera & Garduño-Monroy, 2010; Cabral-Cano et al., 2008; 2010b; Garduño-Monroy et al., 1999; 2001; Lermo-Samaniego et al., 1996; Martínez-Reyes & Nieto-Samaniego, 1990; Osmanoglu et al., 2011; Trejo-Moedano & Martinez-Baini, 1991; Trujillo-Candelaria, 1985).

Morelia is located in the Guayangareo Valley, at an elevation of 1850–2100 m a.s.l. The valley is a lacustrine region, with sedimentary sources both south and north of the valley. To the south, the Sierra de Mil Cumbres (SMC) or Santa María Region comprises a Middle Miocene sequence of rhyolitic pyroclastic flows, andesites and breccias. To the north, monogenetic volcanoes and lava cones of the Michoacán–Guanajuato volcanic field occur as part of the Mexican Volcanic Belt. In the urban area, the following units are defined (Fig. 1; Ávila-Olivera et al., 2010a): Miocene andesites, overlain by a sequence of ignimbrites and pyroclastic flows of the "Cantera de Morelia", also of Miocene age, overlain by Miocene–Pliocene andesites and dacites belonging to the volcanic sequence of Cerro Punhuato. These are overlain by Miocene–Pliocene fluvio-lacustrine deposits and pyroclastic flows, and Pleistocene–Holocene andesites and basalts from Quinceo (2787 m a.s.l.) and Las Tetillas (2760 m a.s.l.) volcanoes, part of the Michoacán–Guanajuato volcanic field. The uppermost units are sedimentary deposits and cemented tuffs of Quaternary age, forming the major aquifer.

Morelia's 16th century buildings have survived remarkably well and represent a type of "strain marker". Until recently, they suggested relative stability of the urban land surface. However, since the 1980s, structural problems began to appear in newly urbanized areas. Differential land subsidence was first recognized in 1983, when small gashes evolved to form a network of normal faults, with average vertical displacement rates of 4–6 cm/yr (Garduño-Monroy et al., 2001). Today, nine major NE–SW and E–W normal faults can be recognized within the urban area: La Colina, Central Camionera, La Paloma, Chapultepec, Torremolinos, El Realito, La Soledad, Cuautla and Ventura Puente (Fig. 1). The orientation of these faults coincides with regional tectonic faults. As described by Garduño-Monroy et al. (1998, 2001), two of these faults, La Colina and La Paloma, have a tectonic origin and are potentially seismic. They are part of the Morelia–Acambay fault system which is in turn related to the Chapala–Tula Fault zone (Johnson & Harrison, 1990). All other faults within the city are likely the result of groundwater extraction, although some may reflect reactivation of pre-existing structures. These latter faults are shallow, mainly affecting Miocene–Pleistocene terrains and sediments but not the underlying ignimbrites. They typically involve narrow damage zones, up to 30–40 m wide (Ávila-Olivera & Garduño-Monroy, 2008;
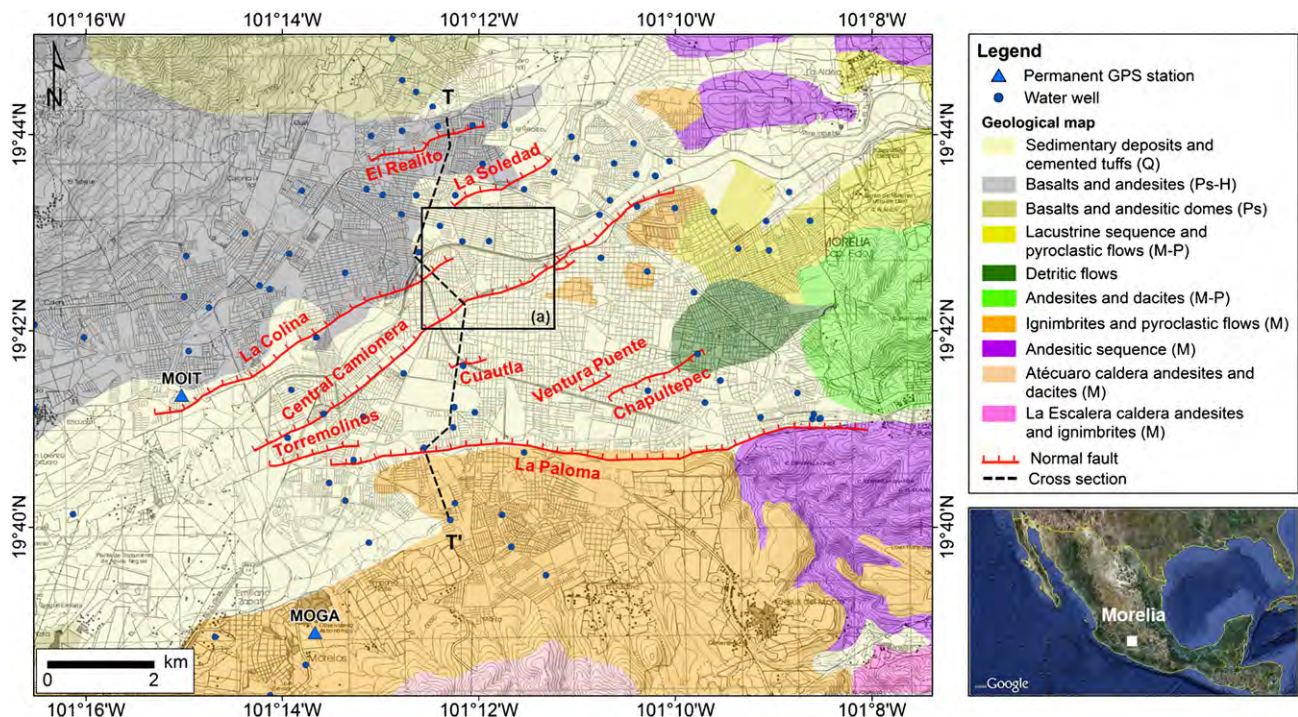

Fig. 1. Location (Google Earth, right inset) and geological map (Ávila-Olivera et al., 2010a) of the city of Morelia, Michoacán, Mexico. Geology is overlaid on a 1998 topographic map (Morelia E14A23; 1:50,000 scale), updated with recent street block information. Location of MOGA and MOIT GPS permanent stations, water wells and cross-section T-T', as well as of the Rio Grande meander area (a), are also represented. Q = Quaternary; Ps = Pleistocene; H = Holocene; P = Pliocene; M = Miocene.

Cabral-Cano et al., 2010a) and have begun to seriously affect the urban infrastructure (Garduño-Monroy et al., 1999).

Extensive geotechnical surveys, including paleo-seismic, Ground Penetrating Radar (GPR) and Seismic Refraction Tomography (SRT) campaigns, and a conventional InSAR study have been carried out in Morelia (Ávila-Olivera & Garduño-Monroy, 2004, 2006, 2008; Ávila-Olivera et al., 2008, 2010b; Cabral-Cano et al., 2010a; Farina et al., 2007, 2008; Garduño-Monroy et al., 2001). These surveys indicate a complex spatial–temporal pattern of fault motion, subsidence, and infrastructure damage.

3. SAR data and interferometric analysis

The causes and patterns of ground subsidence are well known for several cities in the Mexican Volcanic Belt. In Mexico City, pioneering studies initiated decades ago using ground-based techniques documented the extent and cause of subsidence (Carrillo, 1948; Gayol, 1925; Ortega-Guerrero et al., 1993). Recent conventional and advanced InSAR investigations have extended our understanding of this process (e.g., Cabral-Cano et al., 2008, 2010b; López-Quiroz et al., 2009; Osmanoglu et al., 2011; Strozzi & Wegmüller, 1999; Strozzi et al., 2002) by providing detailed coverage of the spatial and temporal variations in subsidence. Here we extend these advanced techniques to Morelia.

Twenty three radar images acquired by the ASAR (Advanced SAR) sensor on board the European ENVISAT satellite, operating in C-band (wavelength 5.6 cm; frequency 5.3 GHz), were acquired for Morelia (Table 1). These scenes span the time interval between July 12th, 2003 and May 1st, 2010 and were acquired in Image Mode S2 (look angle, $\theta = 20.8°$; swath = 100 km), with VV polarization, and along descending orbits (track 69, frame 3213).

Conventional InSAR and Persistent Scatterer Interferometry (PSI) processing were performed using GAMMA SAR software for raw data (Werner et al., 2000). Subsequent steps employed Delft Object-oriented Radar Interferometric Software (DORIS) and the PSI Toolbox (Kampes & Usai, 1999; Ketelaar, 2009; Sousa et al., 2010), both developed by the Delft Institute of Earth Observation and Space Systems of

Delft University of Technology (TU-Delft), and the Automated DORIS Environment (ADORE), developed at the Geodesy Laboratory, University of Miami (Osmanoglu, 2010).

Precise orbits from the Delft Institute for Earth-Oriented Space Research (DEOS) were used to minimize orbital errors for all scenes (Scharroo & Visser, 1998), except the three most recent ones. For these, the Precise Orbit Ephemeris from Centre National d'Etudes Spatiales (Willis et al., 2006) or, if not available, preliminary orbits (Medium-precision Orbit Ephemeris) from the European Space Agency (ESA) were used.

3.1. InSAR analysis

InSAR, in the conventional single-interferogram approach used here, exploits two radar images of the same area acquired at different times to measure ground displacement (Massonnet & Feigl, 1998; Rosen et al., 2000). The technique uses the phase difference of backscattered signals from the two acquisitions to measure differential motion in the Line Of Sight (LOS) direction (e.g., Goldstein et al., 1993; Kimura & Yamaguchi, 2000; Massonnet et al., 1995; Singhroy et al., 1998).

Our InSAR analysis used four SAR pairs with short perpendicular baselines ($B_{perp} < 200$ m) and relatively short temporal baseline ($B_{temp} < 1.5$ yr) in order to minimize the spatial and temporal decorrelation of the corresponding interferograms. These interferometric pairs span the time interval between 2003 and 2009 (Table 2). Interferograms spanning the rainy season (May–August) tended to have strong atmospheric-related artifacts and were avoided.

SAR raw data were first processed and converted to Single Look Complex (SLC) images, maintaining full resolution for each acquisition (i.e. 4 m in the azimuth direction and 20 m in range). The SLCs were then cropped to our study area of 20 km by 16 km, including both the urban and suburban sectors of Morelia. After co-registration of slave images to their respective masters, a multi-look ratio of 5:1 (final pixel size 20 m by 20 m) was used to generate raw interferograms and subsequent products.

Extraction of the displacement phase component from each of the raw interferograms was carried out using the 'two-pass interferometry' approach (Massonnet & Feigl, 1998). Subtraction of topographic information from each interferogram was performed using a pre-existing Digital Elevation Model (DEM) to simulate the synthetic topographic phase. We used the 30 m resolution ASTER Global DEM, distributed by NASA's Land Process Distributed Active Archive Center.

We applied an adaptive filtering to each differential interferogram (Goldstein & Werner, 1998) to reduce phase noise and improve subsequent 2D phase unwrapping. We then used the Statistical-cost, Network-flow Algorithm for PHase Unwrapping (SNAPHU) approach (Chen & Zebker, 2000) to resolve ambiguous wrapped phase data. Connected component masks (i.e. pixels unwrapped in a relative, internally self-consistent manner), derived from the four unwrapped solutions, were also applied to the unwrapped interferograms to limit subsequent processing steps to reliable areas. The unwrapped differential phases were then converted into four maps of ground displacement (measured along the satellite LOS) and geocoded according to the ASTER DEM projections.

The final results of the InSAR processing were also converted from maps of LOS displacements into maps of time-normalized LOS deformation rates, based on the time span of the respective interferogram.

Table 1
Baseline information for ENVISAT ASAR IS2 descending data for Morelia: perpendicular (B_{perp}) and temporal (B_{temp}) baselines, and Doppler centroid frequency differences (B_{dopp}) between master and each slave acquisition. Master image for PSI processing is 22 January 2005.

Date	B_{perp} [m]	B_{temp} [days]	B_{dopp} [Hz]
12 Jul 2003	−753.8	−560	62.4
16 Aug 2003	−806.9	−525	29.7
7 Feb 2004	158.7	−350	5.4
13 Mar 2004	655.0	−315	11.0
17 Apr 2004	476.3	−280	8.5
31 Jul 2004	191.9	−175	13.3
13 Nov 2004	−743.5	−70	1.7
18 Dec 2004	−371.8	−35	0.8
22 Jan 2005	0	0	0
7 May 2005	805.0	105	9.4
11 Jun 2005	−280.6	140	2.0
16 Jul 2005	813.0	175	12.7
20 Aug 2005	81.0	210	11.6
3 Dec 2005	−431.8	315	20.0
11 Feb 2006	−542.9	385	28.8
27 May 2006	−624.0	490	22.2
23 Dec 2006	185.5	700	29.1
27 Jan 2007	−346.3	735	25.2
27 Dec 2008	−74.0	1435	24.7
3 Oct 2009	−85.9	1715	33.0
20 Feb 2010	−164.2	1855	35.9
27 Mar 2010	172.1	1890	21.7
1 May 2010	148.1	1925	22.6

Table 2
Temporal (B_{temp}) and perpendicular (B_{perp}) baselines for ENVISAT InSAR pairs.

Pair ID	Dates	B_{temp} [days]	B_{perp} [m]
A	12 Jul 2003–13 Nov 2004	490	10.3
B	18 Dec 2004–3 Dec 2005	350	−60.0
C	11 Feb 2006–27 Jan 2007	350	196.6
D	27 Dec 2008–3 Oct 2009	280	−11.9

This allows us to directly compare our displacement rate estimates to those obtained by other techniques with slightly different time spans and to highlight differences in the four time interval maps.

The choice of the location for the zero deformation point (reference location, set to zero velocity) for the relative displacement maps was driven by the following criteria: i) high coherence values in the interferograms; ii) location south of La Paloma fault which is an area that we assumed to be devoid of large subsidence displacements due to its outcrop lithology (Fig. 1); iii) close proximity to the MOGA GPS station whose vertical time series exhibits stable behavior (see Section 4.1.1); and iv) same outcropping lithological unit as MOGA station (Fig. 1).

In the following sections, deformation is evaluated along ENVISAT LOS, a direction that is nearly E–W. A single acquisition geometry cannot resolve all 3 orthogonal components of ground deformation vectors. However, if we assume that ground displacement in Morelia occurs only in the vertical direction, two boundary conditions are set (azimuth and dip of displacement vector) and the magnitude of pure vertical deformations can be estimated. Thus, LOS measurements (d_{LOS}) can be converted to vertical displacements (d_V) following the relation $d_V = d_{LOS}/cos\theta$; this conversion corresponds to a modification (increment) of the LOS measurement by about 7%.

3.2. Persistent Scatterer analysis

As a complement to the conventional InSAR study, a multi-interferometric analysis was carried out using the Delft Persistent Scatterer Interferometry (DePSI) technique, developed at TU-Delft (Kampes & Usai, 1999; Ketelaar, 2009; Sousa et al., 2010). Unlike InSAR, PSI analyses use multi-temporal stacks of SAR images to generate time-series of ground deformations for individual radar targets (i.e., the Persistent Scatterers, PS), subject to the condition that a model for the

time history of deformation (e.g., linear deformation) is assumed (e.g., Bürgmann et al., 2006; Crosetto et al., 2010; Dixon et al., 2006; Ferretti et al., 2001; Hanssen, 2005; Hilley et al., 2004; Hooper et al., 2004; Kim et al., 2010; Werner et al., 2003). The density of measures within the displacement maps is increased substantially (up to several hundreds of PS per km² may be identified) and a more detailed analysis of local patterns of land subsidence can be performed.

The DePSI analysis used available ENVISAT scenes covering the time interval 2003–2010. The image acquired on January 22nd, 2005 was selected as the master, to minimize the effects of spatial and temporal decorrelation and to avoid any possible atmospheric contributions potentially present during the rainy season (May–August). The resulting perpendicular baselines range between ± 820 m, while temporal baselines range between −560 and +1925 days (Table 1).

The area investigated with PSI corresponds to that analyzed with conventional InSAR. All the SLCs were cropped to the same area and oversampled by a factor of two in both range and azimuth, to prevent undersampling of the data during resampling of the slave acquisitions to the master geometry and subsequent creation of the interferograms. Thus each resolution cell was resized to half the size of SLC radar pixels (4 m by 20 m), i.e. approximately 2 m by 10 m.

First order PS Candidates (PSC) and PS Potential (PSP) were selected using the amplitude dispersion criterion (Ferretti et al., 2001). Points characterized by amplitude dispersion index, D_A, higher than a given threshold were excluded from further processing. We used a threshold of 0.3 and 0.4, for PSC and PSP respectively.

Limited temporal sampling, averaging twenty three scenes in six years, precluded a rigorous analysis of temporal variation. We assumed a linear model of phase variation through time for both PSC and PSP, for estimation of phase components related to deformation. This choice was driven by the linear deformation behavior observed
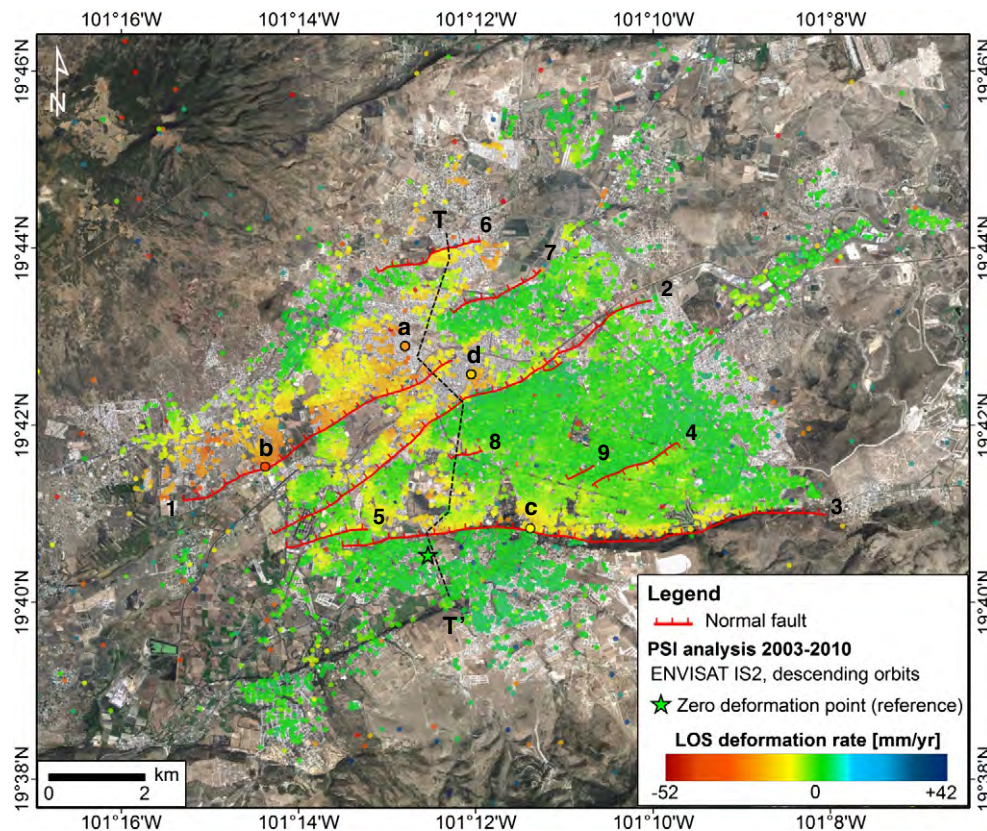

Fig. 2. LOS deformation rates in Morelia between 2003 and 2010, obtained through the PSI analysis of 23 ENVISAT images acquired along descending orbits (see Table 1 for temporal and perpendicular baseline distribution). PSI map is overlaid on Google Earth imagery. Location of cross-section T–T′ is also represented. Normal faults: 1, La Colina; 2, Central Camionera; 3, La Paloma; 4, Chapultepec; 5, Torremolinos; 6, El Realito; 7, La Soledad; 8, Cuautla; 9, Ventura Puente. Time series for selected PS *a*, *b*, *c* and *d* are shown in Fig. 3.
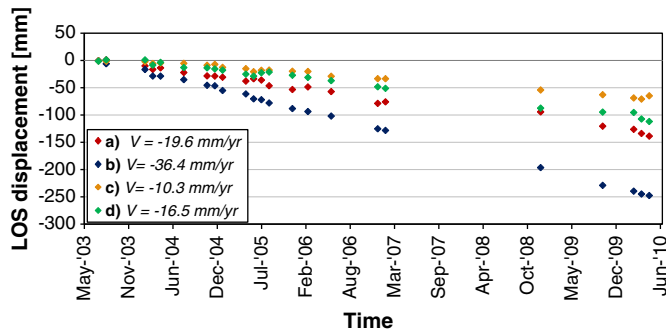
Fig. 3. LOS displacement time series and yearly velocities of PS *a*, *b*, *c* and *d* (Fig. 2), located north of La Colina, La Paloma and Central Camionera faults. Time series are rescaled to the first acquisition (i.e. 12 July 2003).

between 1980 and 1997 on the La Colina fault, based on conventional leveling and evidence from historical photographs (Garduño-Monroy et al., 2001). For more than 90% of the area, a simple linear model for deformation fits the phase data extremely well; exceptions are noted below.

The reference point for the PSI analysis was selected in the same location as for the InSAR displacement maps, in order to make the PSI deformation values consistent and easily comparable to those from the InSAR analysis. As with the InSAR analysis, PSI deformation values are evaluated along the ENVISAT LOS and can be converted to vertical displacement or velocity, modifying the LOS measurement by about +7%.
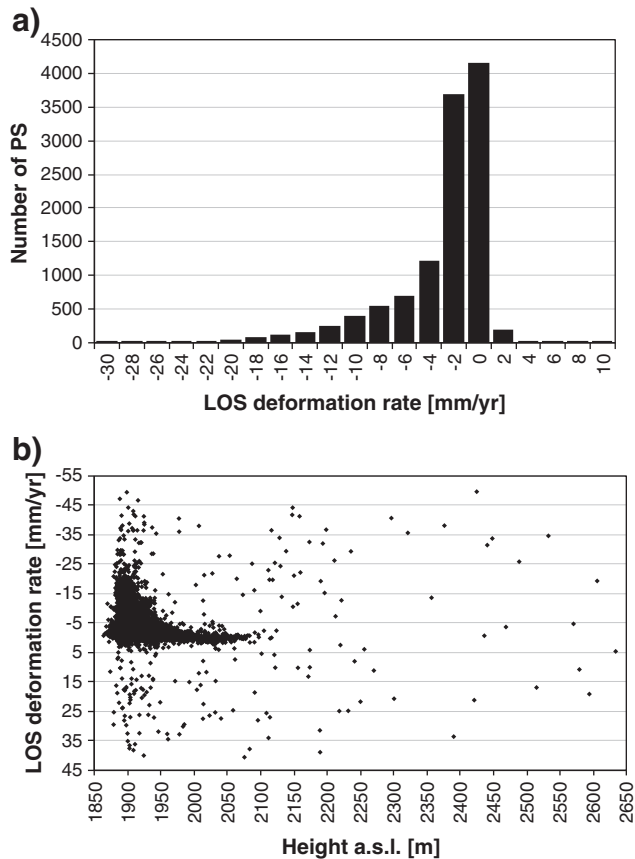

Fig. 4. Histogram of LOS deformation rates observed in Morelia in 2003–2010 (a), limited to the velocity range from −30 to +10 mm/yr. Each class of the histogram spans an interval of ±1 mm/yr, to each side of the value shown in the x-axis. Comparison of LOS deformation rates in 2003–2010 with elevations for individual PS for the complete PSI dataset (b).

4. Results

4.1. Analysis of average subsidence with PSI

The DePSI processing identified more than 11,800 PS in the study area (320 km^2), with a mean point density of 37 PS/km^2 and a maximum density (in the urban area) up to about 300 PS/km^2. Average annual deformation rates in 2003–2010 and selected time series of PS belonging to relevant sectors of the city are shown in Figs. 2 and 3 respectively. Time series are rescaled to the first acquisition date (i.e. 12 July 2003), being understood that the PSI master image (temporal reference) of the processing is the 22 January 2005 acquisition. A large
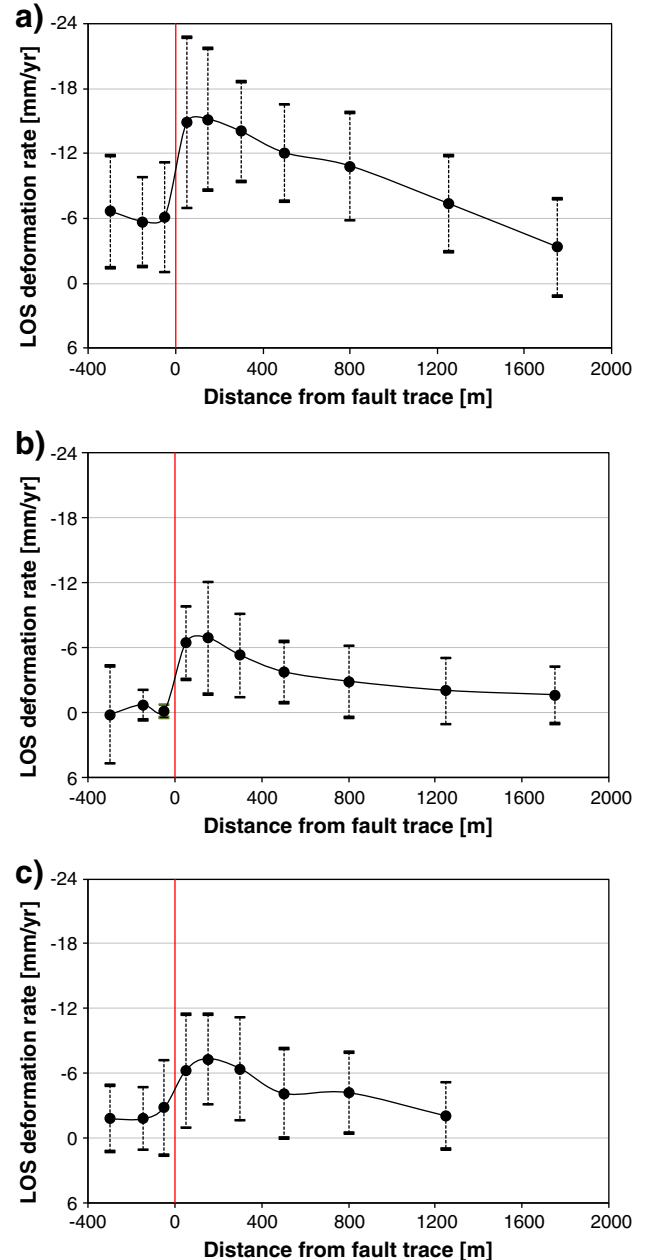

Fig. 5. Average LOS deformation rates measured in 2003–2010 at different distances from the fault traces of La Colina (a), La Paloma (b) and Central Camionera (c) faults. Deformation rates are averaged for different buffer areas defined by their distance from each fault trace. Standard deviations of average estimations are also shown. Vertical line marks fault location; positive distances are referred to the hanging wall sides of each fault.

portion of the urban developed area shows very low LOS deformation rates, ranging between 0 and 2 mm/yr (close to the PSI technique detection sensitivity), and indicating stability in those parts of the city. However, high subsidence rates are observed near several fault traces, e.g., the hanging wall side of La Colina, Central Camionera, La Paloma, Torremolinos, Cuautla and Chapultepec faults. Fig. 4a shows that the

LOS deformation rates are strongly skewed to negative values, consistent with the idea that groundwater-related subsidence is the dominant process, but rates between ±1 mm/yr are the most common values, suggesting that much of the region is not yet experiencing significant overdraft. Fig. 4b compares the LOS deformation rates to the elevation of individual scatterers. A few (much less than 1%) of the
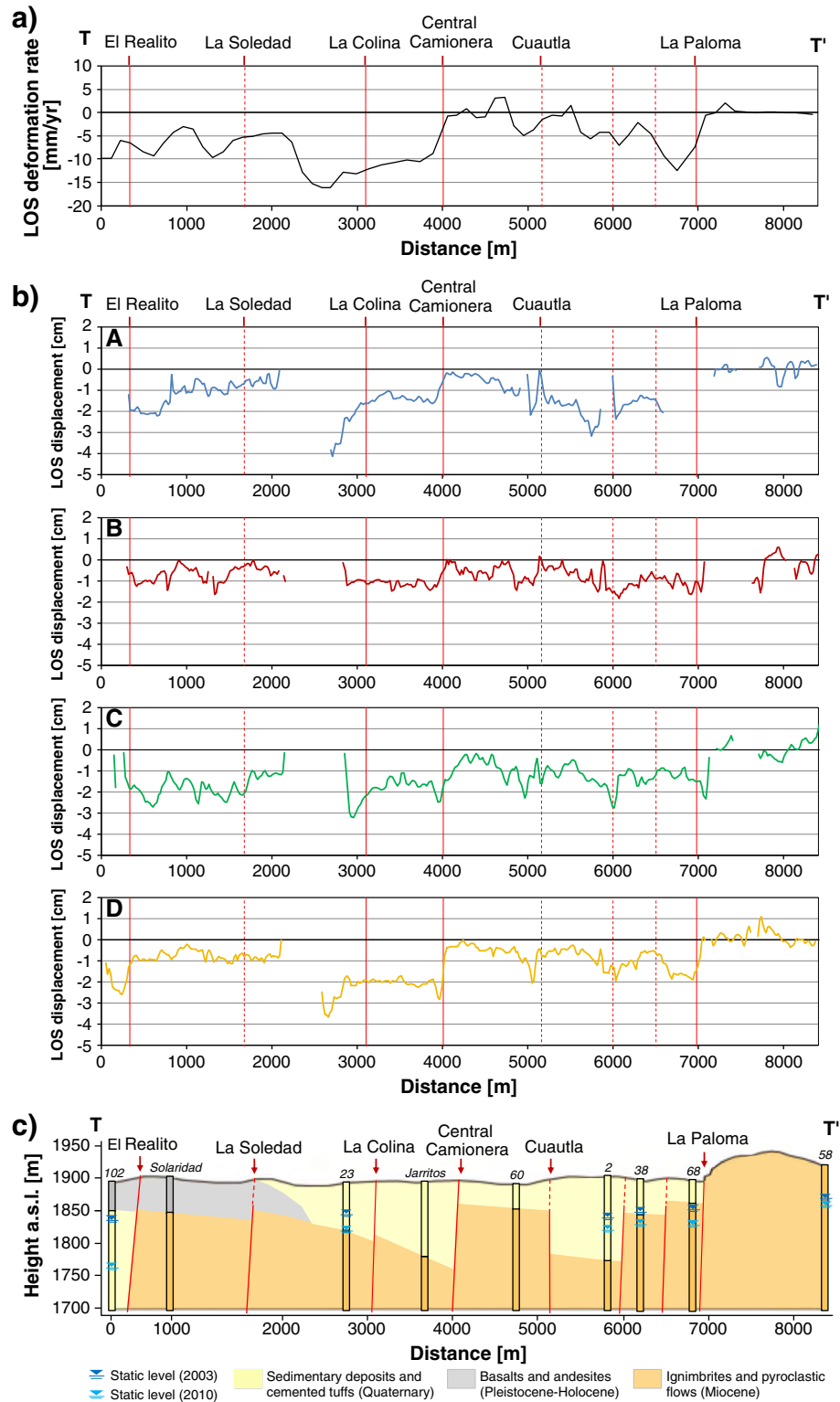

Fig. 6. Profile of 2003–2010 PSI deformation rates (a) and 2003–2009 LOS displacements from the InSAR time-lapse analysis (b) along the T–T′ geological cross section (c), whose location is shown in Fig. 1. Main faults are represented with red lines (solid = confirmed by field surveys; dashed = inferred). Static level in 2003 (interpolated) and 2010 (extrapolated) are also represented.

points exhibit extreme scatter, presumably reflecting noise. This is clearly random, with no evidence of systematic bias in either deformation rate or elevation estimates. The most common (zero) deformation rate is observed over a wide range of elevations, and there is no correlation between rate and elevation for these points. However, the negative (subsidence) rates all occur at low elevations. This is also consistent with the idea that groundwater-related compaction is the dominant process, as we expect the main aquifers to be located in low-lying alluvial basins.

A clearly imaged displacement gradient across each fault is observed. All these structures dip north, with the exception of Chapultepec, which dips south (Fig. 1). The highest deformation is concentrated on the north side (i.e. hanging wall) of these faults, with the exception of the Chapultepec fault, where highest deformation occurs on the south side, due to its opposite orientation. In all these areas, ground deformation progressively decreases along dip as a function of distance from the fault trace.

It is useful to define a zone of high deformation (>5 mm/yr) extending some distance to each side of the fault, to guide hazard assessments for civil infrastructure. We term this the 'high deformation band' and where possible, give its total width perpendicular to the fault based on the PSI analysis. To facilitate the identification of the high deformation band, average deformation rates for different buffer areas defined by their distance from each fault trace (e.g., 0–100 m, 100–200 m, 200–400 m, 400–600 m, to both the hanging walls and the footwalls) were also calculated for La Colina, La Paloma and Central Camionera faults (Fig. 5).

North of La Colina, observed LOS subsidence rates are 20–30 mm/yr, with a few points exceeding 50 mm/yr (Figs. 2 and 3a and b). The width of the high deformation band is 1200–1500 m on the fault hanging wall, with average rates of 15–20 mm/yr near the fault trace; on the footwall, the high deformation band of this fault is 100 m and, to the south, overlaps with that of Central Camionera. Visual reconnaissance of obvious damage to civil infrastructures had previously identified only a 20–25 m wide zone of influence (i.e. zone of fault-induced structural damage) while shallow geophysical investigations show a zone of closely-spaced shallow faulting up to 40 m from each side of main fault trace (Ávila-Olivera & Garduño-Monroy, 2008; Cabral-Cano et al., 2010a; Garduño-Monroy et al., 2001). This apparent inconsistency may be a consequence of the more recent SAR observations.

North of La Paloma, maximum LOS deformation rates are up to 10–15 mm/yr (Fig. 3c). For this fault the high deformation band extends only to the hanging wall, and ranges between 300 m on the eastern sector and 500 m on the western sector of the fault trace. North of the Torremolinos fault, displacement rates range between 5 and 10 mm/yr, while north of the Cuautla and south of the Chapultepec faults the maximum observed rates are near 5 mm/yr.

Rates of 15–20 mm/yr of LOS displacement are also measured within a small area southeast of the El Realito fault, corresponding to its footwall. Here geological surveys carried out by the water management agency of Morelia, OOAPAS (*Organismo Operador de Agua Potable, Alcantarillado y Saneamiento*), show a total thickness of compressible sediments of 215 m, decreasing to 10–20 m thickness 500 m to the south. The thicknesses of these sediments were obtained by analyzing core samples from water well construction, and calculating the total amount of the compressible layer – for each core sample – as the sum of all the contributions from the lacustrine sediments comprising the core. On the other side, in the hanging wall of the El Realito fault, very few PS were identified and no clear pattern of deformation can be deduced (Fig. 2); however, compressible material thicknesses measured here are very similar to those of the footwall, leading us to infer deformation rates similar to those measured south of the fault.

In the area north of the Central Camionera fault, no more than 15–20 mm/yr of LOS deformation rates are observed close to the hanging wall (Fig. 3d), where the thickness of compressible sediments is about 120–150 m (in the footwall this is only 30–50 m). Field observations

Table 3
LOS deformation rates observed along the cross-section T–T′ for hanging walls (H) and footwalls (F) of normal faults in Morelia (Fig. 6b); 2003–2010 PSI rates and 2003–2009 InSAR time-lapse velocities are referred to buffer areas 500 m wide to each side of the faults. Temporal and perpendicular baselines of InSAR pairs are summarized in Table 2.

Fault		Average LOS deformation rates [mm/yr]				
Name	Side	PSI	InSAR (A)	InSAR (B)	InSAR (C)	InSAR (D)
La Colina	H	−11.1	−19.9	−9.6 [a]	−25.0 [a]	−33.5
	F	−12.7	−9.8	−11.6	−16.9	−25.6
Central Camionera	H	−9.8	−10.2	−11.9	−17.8	−28.1
	F	−0.5	−2.1	−5.0	−7.1	−4.3
La Paloma	H	−8.4	−12.8	−11.1	−12.3	−18.6
	F	0.4	0.0	−10.6 [a]	−5.6	−0.5
El Realito	H	−8.0	−9.0 [a]	−5.4 [a]	−12.1 [a]	−26.5
	F	−7.1	−13.9	−9.7	−20.9	−11.3
La Soledad	H	−7.4	−6.6	−8.4	−21.1	−11.2
	F	−4.6	−4.2	−4.8	−12.5	−10.6
Cuautla	H	−1.1	−7.5	−7.0	−13.4	−11.2
	F	−1.1	−12.0	−5.6	−9.9	−7.0

[a] Lack of measures exceeding 60% of the buffer and/or presence of outliers.

identified about 80 cm of fault offset between 1983 and 2001 (equivalent to about 4.5 cm/yr if the deformation rate is constant) and a zone of influence of ~40 m (Ávila-Olivera & Garduño-Monroy, 2008). The width of the PSI-defined high deformation band for this fault is about 500 m to the hanging wall, while average rates lower than 3 mm/yr are observed in the footwall (Fig. 5); however, reliability of this estimation is poor due to temporal decorrelation and consequent lack of PS in this area.

A low density of PS also occurs in the Rio Grande meander area, for which well-marked and very high displacements were identified with the InSAR analysis (see Section 4.2.1). This may reflect the temporal evolution of ground displacement here, where deformation appears to be accelerating, such that the linear model applied successfully in other regions may not apply.

A deformation profile of PS data was analyzed along transect T–T′ (Fig. 6a and Table 3). This profile was extracted using an Inverse Distance Weighting spatial interpolation (with a resampled cell size of 100 m by 100 m) of the observed annual PSI displacement rates (Fig. 2) together with a geological cross-section derived from geological reconnaissance (Fig. 1). Significant differences are observed in adjacent areas of the city. Across the La Paloma and Central Camionera faults, a sharp increase of about 10–12 mm/yr (i.e. 7–8 cm in the 2003–2010 period) in the deformation field is observed. This behavior is mostly restricted to the hanging wall of each fault. In the area between the La Colina and La Soledad faults, a sharp change of 12 mm/yr is also observed in the deformation profile.
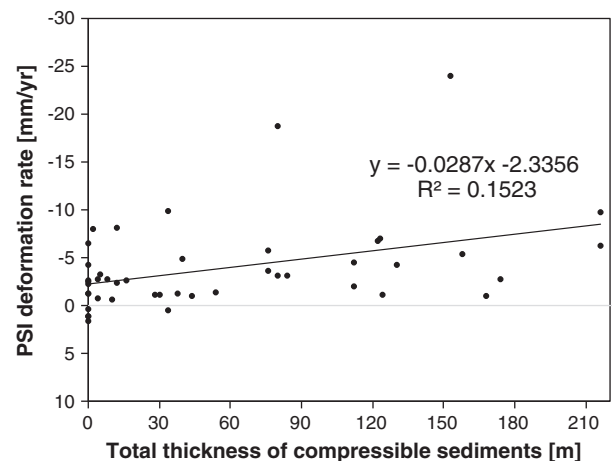

$$y = -0.0287x - 2.3356$$
$$R^2 = 0.1523$$

Fig. 7. Comparison of 2003–2010 PSI-based subsidence estimates with total thickness of compressible sediments for major well locations.

Table 4
Comparison of water extraction data and PSI measures in Morelia: construction date, pumping rate, static levels, water table change, and respective 2003–2010 deformation velocities. Respective measurement dates are also shown for extraction rates and static levels. N.C., Not Computable (less than two measurements available).

Id	Constr. date	Extraction rate [l/s]	Static level [m] First measure	Static level [m] Last measure	Static level drop [m/yr]	LOS rate [mm/yr]
1	1980	34 (2007)	74 (1991)	103 (2003)	2.42	−3.67
2	1973	63 (2006)	13 (1974)	74 (2006)	1.91	−7.04
3	1980	36 (1996)	49 (1989)	116 (2006)	3.94	−2.33
4	1999	30 (2005)	7.5 (1999)	24 (2005)	2.75	−1.18
5	1980	27.1 (2006)	25.7 (1980)	65 (2003)	1.71	−6.67
6	1975	28 (2005)	19.5 (1990)	40 (2003)	1.58	−4.51
7	1999	4 (1999)	10 (1999)	79 (2008)	7.67	0.30
9	1993	17.7 (2008)	27.6 (1993)	141 (2005)	9.45	−3.14
11	1985	40 (2005)	10 (1985)	48 (2000)	2.53	−5.31
13	1997	15.4 (2000)	36 (1997)	–	N.C.	−2.06
16	1993	8 (2001)	20.5 (1999)	22.5 (2005)	0.35	−6.76
19	2000	18 (2007)	58 (2000)	92 (2007)	4.86	−2.62
20	2000	6 (2001)	77 (2000)	114 (2006)	6.17	−0.55
21	2000	26.4 (2007)	23.5 (2000)	137 (2007)	16.21	−2.48
22	1984	18.5 (2002)	60 (1984)	89 (2006)	1.32	1.12
23	1998	10.6 (2007)	39 (1998)	63 (2006)	3.00	−18.83
24	1989	9 (1992)	28.4 (1989)	30 (1992)	0.53	−2.04
25	1992	3 (1999)	14 (2009)	–	N.C.	−8.06
26	1982	6.79 (1990)	40.5 (1982)	96 (2002)	2.78	−0.34
27	1988	9 (2006)	16 (1988)	133 (2006)	6.50	−1.15
28	1986	5.3 (2006)	7 (1986)	36 (2006)	1.45	−1.18
29	1987	15 (1992)	62 (1987)	114 (2005)	2.89	−2.73
30	1991	37.3 (1992)	27 (1992)	–	N.C.	−6.57
31	1987	9.2 (2008)	23 (1987)	113 (2008)	4.29	−1.62
33	1990	18.2 (1997)	34 (1990)	44 (2007)	0.59	−1.18
34	2001	14.5 (2006)	32 (1993)	42 (2002)	1.11	0.00
35	1996	–	78 (1996)	102 (2003)	3.43	−1.03
36	1989	26 (2008)	19 (1989)	64 (2008)	2.37	−0.99
37	1989	24 (2005)	92 (1989)	139 (2004)	3.13	−0.69
38	1988	6 (2005)	6 (1989)	54 (2005)	3.00	−2.01
39	1989	45 (1989)	20 (1989)	–	N.C.	−5.78
40	1989	10 (2005)	25.5 (1993)	40 (2005)	1.21	−1.22
41	1990	43 (2005)	38 (1990)	70.5 (2005)	2.17	−3.17
42	1991	9 (2005)	72 (1994)	165 (2003)	10.33	−4.92
43	1991	2.1 (2007)	34 (1991)	132 (2005)	7.00	−2.02
44	1997	–	42 (2001)	45 (2003)	1.50	−4.40
45	1996	7.3 (2008)	39.6 (1996)	48 (2008)	0.70	−18.72
46	1990	8.3 (1997)	17.4 (1990)	42 (2005)	1.64	−1.40
47	1992	11 (1992)	2 (1992)	–	N.C.	−6.07
48	2000	10 (2002)	12 (2002)	81 (2005)	23.00	−0.58
49	1992	18 (2001)	0 (1992)	68 (2001)	7.56	−0.52
51	1994	10 (2004)	38 (1995)	84 (2005)	4.60	−1.45
52	1999	4 (2007)	41 (2000)	–	N.C.	−1.02
53	2004	6 (2005)	110 (2004)	–	N.C.	−1.64
54	1991	6.6 (1994)	106 (1991)	147 (2004)	3.15	−0.78
55	1992	8 (2005)	68.9 (1992)	142 (2007)	4.87	−1.03
56	1995	40 (2008)	40 (2005)	–	N.C.	−0.94
58	1995	21 (2008)	33 (1995)	49 (2005)	1.60	1.02
63	2001	35.3 (2007)	68 (2000)	97 (2005)	5.80	−3.39
64	1993	16 (2002)	50 (1993)	84 (2002)	3.78	−5.36
65	1987	8 (2007)	25 (1988)	26 (2001)	0.08	−10.76
66	1990	28 (2006)	20 (1990)	54.5 (2005)	2.30	−26.07
68	1994	18 (2008)	0 (1994)	33 (2002)	4.13	−9.92
69	1984	4 (2008)	70 (1984)	181 (2008)	4.63	0.71
70	2001	2 (2008)	22 (2001)	27 (2007)	0.83	−7.06
72	1996	24 (1996)	15 (1996)	–	N.C.	−2.36
73	2002	11 (2002)	66 (2002)	–	N.C.	−26.73
74	1996	–	123 (1998)	154 (2004)	5.17	−1.04
76	2007	8 (2007)	100 (2007)	–	N.C.	−6.56
77	1990	9 (1999)	42.5 (1990)	49.5 (2006)	0.44	−4.48
78	2001	29 (2005)	81 (2002)	–	N.C.	−2.60
79	2000	4 (2002)	76 (2000)	93 (2003)	5.67	0.42
88	1999	6.3 (2006)	72 (1999)	–	N.C.	−7.06
89	1999	9 (2008)	18 (1999)	89 (2008)	7.89	−2.83
90	1999	8.6 (2006)	65 (1999)	121 (2006)	8.00	−10.01
91	2000	27 (2005)	38 (2001)	–	N.C.	−2.51
92	2000	2 (2007)	43.5 (2000)	116 (2007)	10.36	−1.70
93	2000	28 (2003)	20 (2001)	–	N.C.	−6.74
94	2000	28 (2001)	87 (2001)	96 (2008)	1.29	−4.30
95	2000	2.5 (2008)	15 (2000)	214 (2006)	33.17	6.49
96	2000	3 (2002)	117 (2000)	120 (2002)	1.50	−2.83

Table 4 (continued)

Id	Constr. date	Extraction rate [l/s]	Static level [m] First measure	Static level [m] Last measure	Static level drop [m/yr]	LOS rate [mm/yr]
98	2000	24 (2007)	108 (2000)	128 (2007)	2.86	−3.28
99	2000	9 (2008)	85 (2000)	87 (2002)	1.00	1.63
100	2000	21.7 (2007)	14 (2001)	85 (2007)	11.83	−6.56
101	2000	15 (2001)	17 (2001)	–	N.C.	−6.56
102	1991	3.8 (2007)	21 (1999)	84 (2005)	10.50	−9.74
103	2000	24 (2008)	47 (2001)	83 (2004)	12.00	−2.55
105	2000	17 (2001)	148 (2001)	167 (2005)	4.75	−1.32
106	2001	18.8 (2006)	42 (2002)	–	N.C.	−1.37
107	2000	19.3 (2008)	92 (2001)	119.5 (2005)	6.88	−1.36
108	2000	22 (2001)	14 (2000)	–	N.C.	−6.28
110	2001	20 (2004)	18 (2001)	36 (2004)	6.00	−8.18
111	2001	25.3 (2004)	48 (2001)	138 (2008)	12.86	−3.33
114	2001	18 (2001)	41 (2001)	53 (2004)	4.00	−6.73
115	2000	22 (2006)	14 (2000)	–	N.C.	−4.30
116	1995	50 (2002)	89 (1995)	115 (2007)	2.17	−4.30
117	2002	15 (2008)	36 (2002)	–	N.C.	−4.51
119	2000	25 (2003)	–	–	N.C.	−1.55
122	2001	6 (2007)	108 (2001)	126 (2005)	4.50	−3.33
123	2002	12 (2002)	150 (2002)	–	N.C.	−2.33
124	2002	31.6 (2002)	143 (2003)	–	N.C.	−1.32
125	2002	10.5 (2006)	15 (2002)	–	N.C.	−2.36
127	2002	10.3 (2007)	54.8 (2002)	110 (2005)	18.40	−3.69
128	1999	5.4 (2005)	127 (1999)	–	N.C.	−0.83
129	2000	7.4 (2006)	113 (2002)	133 (2006)	5.00	−24.07
131	2001	5.8 (2005)	42 (2001)	–	N.C.	−26.98
133	2004	38 (2004)	–	–	N.C.	−24.07
134	1997	8.2 (2007)	56 (1997)	81 (2004)	3.57	2.79
136	2004	18 (2005)		47.5 (2004)	N.C.	−24.07
137	2004	7 (2006)	31 (2005)	39.5 (2006)	8.50	−5.20
138	2001	19.15 (2006)	17 (2002)	65 (2006)	12.00	−16.43
139	2001	15.55 (2001)	53 (2001)	–	N.C.	−17.93
140	2005	–	33 (2005)	–	N.C.	−0.25
141	2005	41 (2006)	–	–	N.C.	−1.12

To highlight any correlation between greater subsidence and the thickness of the compressible sediments throughout the whole urban area, PS deformation data were compared with the spatially variable thickness of the compressible layers, considering both the shallow and the deeper deposits. The scatter diagram in Fig. 7 shows only a weak correlation between the calculated thickness of total compressible deposits and the occurrence of higher subsidence rates (coefficient of determination, R^2 for the linear regression is about 0.15).

4.1.1. Comparison of well data to PSI data

Water supply in Morelia is managed in the framework of the Pátzcuaro-Cuitzeo sub-basin and is based on the exploitation of both surface (about 65%) and underground (35%) water resources. Potable water demand is met as follows: 108 subterranean water wells distributed throughout the entire urban area, more than half of which were built or reactivated in the last 15 years (approximately 40% of potable water supply); 3 springs (San Miguel, La Minzita and La Higuera y El Salto; 30% of potable supply) and 1 reservoir dam (Cointzio; remaining 30%).

Together with a remarkable increase of the total inhabitants of the city (estimated to be 608,049 during the 2005 census; more than ten times the population of the early '50s), water availability is drastically decreasing, from 4900 m^3/yr per inhabitant in 1999, to 3500 m^3/yr per inhabitant expected by 2025, as identified by the National Water Commission, *Comisión Nacional del Agua*. Water deficiency is expected in the short term, due to urban sprawl, overexploitation of aquifers, and lack of appropriate planning for the safeguarding of supply resources and recharge areas.

Land subsidence estimates in 2003–2010 imaged through the PSI analysis were compared and integrated with groundwater extraction data distributed by OOAPAS, to quantify the correlation between greater subsidence and stronger water extractions. Compaction of

the aquifer system depends not only on the compressibility of the fine-grained deposits, but also on the water head change, so both the presence of significant total thickness of fine-grained deposits in the saturated portion of the aquifer system and the static level declines are needed to manifest compaction.

Measured water extraction rates, static water levels (i.e. depth to water below land surface) and water level drops are summarized in Table 4; the distribution of water extraction rates within the urban area is also shown in Fig. 8. These measures are referred to the most recent updates available up to May 2008, and hence are not exactly contemporaneous with the deformation data. Fig. 9 compares the extraction rates and static level decreases with the 2003–2010 LOS deformation data. The representative PS for the water wells are chosen as the closest radar targets to the respective water extraction sites. Static level decreases are calculated, for each well, in terms of meters of level drop per year (m/yr), assuming a linear variation in time between the first and the last available static level measurement.

We used a modified linear regression to describe the variation of deformation with water extraction rates, excluding from the regression any points with displacement rates more than ±15 mm/yr; this is done to reduce the influence of a few points with very high subsidence rates, often due to location near major extraction wells. Points excluded from the fit are shown in the figure with different symbols. However, even with these points omitted, there is remarkably poor correlation between subsidence and water extraction rates (R^2 for the linear regression is 0.02; Fig. 9a), and no correlation between subsidence and static level decrease (Fig. 9b). The observed weak correlation of PSI deformation with water extraction rates may be consistent with the hypothesis that compaction of deeper aquifers, communicating with shallow ones, exerts significant control on land deformation and imparts uniform subsidence throughout the urban area, upon which local influences are superimposed at a few locations.

4.1.2. Integration of PSI and GPS observations

Integrating InSAR with GPS combines the high spatial density of InSAR measures with the excellent temporal sampling of GPS data. Two GPS stations in Morelia, MOIT and MOGA (Fig. 1), have operated since 2009 and 2008 respectively. The MOGA station is located SW of the La Paloma fault, over Miocene ignimbrites and pyroclastic flows
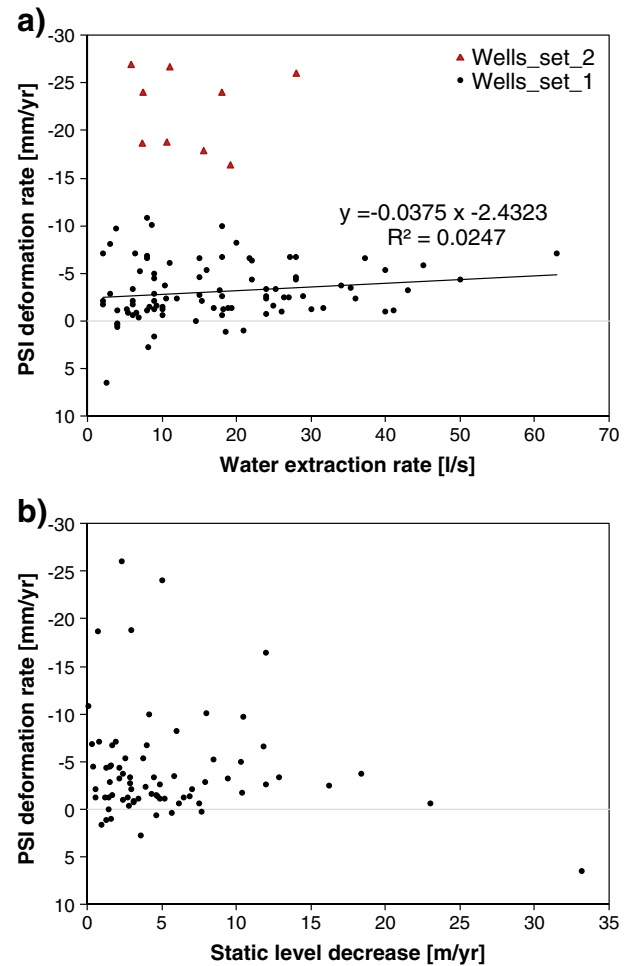
Fig. 9. Comparison of PSI deformation estimates with water extraction rate (a) and static level decrease (b). Linear regression in (a) has been calculated for a subset of more correlated points (black dots).
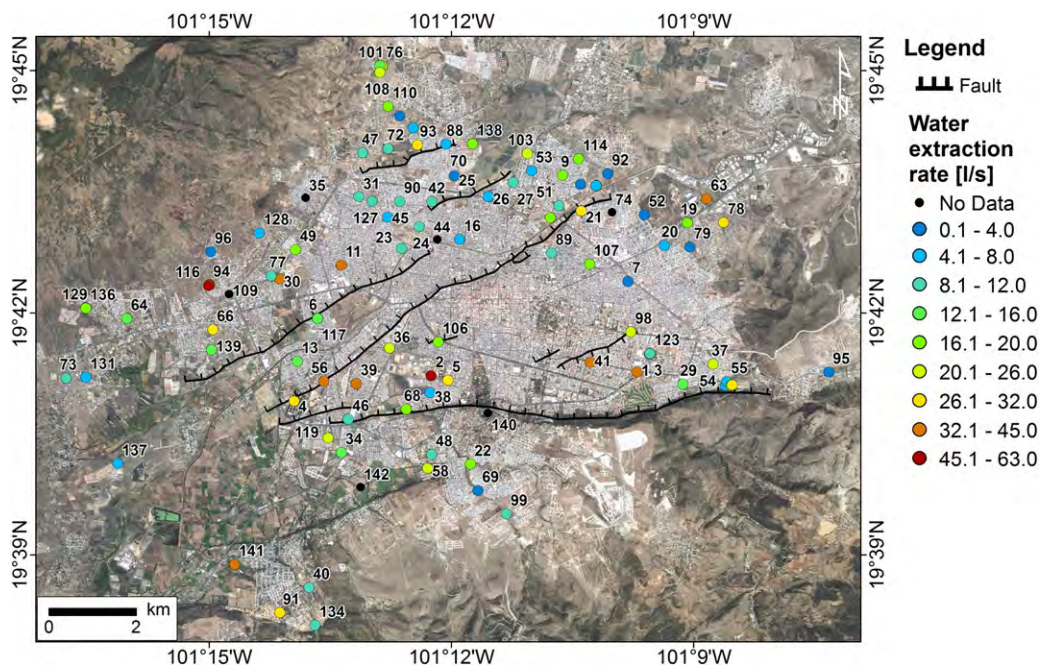
Fig. 8. Water extraction rates measured in Morelia. Water well identification codes are also shown. No Data = no in situ measurement available.

outcrops; it can therefore be considered stable and outside the area of subsidence. The MOIT GPS station is located very close to the western segment of the most active fault, La Colina.

The GPS vertical component time series were compared with the longer PSI time series. The GPS coordinates for each station were determined using standard precise point-positioning analysis of the raw code and phase data using GIPSY-OASIS software from the Jet Propulsion Laboratory, JPL (Webb & Zumberge, 1997). Daily station coordinates were estimated in a non-fiducial reference frame and then transformed to the International Terrestrial Reference Frame ITRF-2005 using daily seven-parameter Helmert transformations from JPL (Altamimi et al., 2007). Representative PS for MOGA and MOIT stations were chosen as the closest radar targets to each station (PS_{MOGA}–GPS_{MOGA} distance = 135 m; PS_{MOIT}–GPS_{MOIT} distance = 115 m). The offset between the GPS and PS time series was removed by adjusting the GPS time series to fit the PSI time series at an arbitrary early time (22 January 2005; Fig. 10).

The integrated time series of vertical displacements show a good agreement between PSI and GPS measures for station MOGA, even given the different time spans covered by these data (2003–2010 and 2008–2011 respectively; Fig. 10a). Within the time series, deviations of PSI measures with respect to GPS monthly averages range between 1 and 2 mm, and the respective yearly deformation rates are very similar: −0.2 mm/yr and −0.7 mm/yr. This agreement is consistent with our assumption of mainly vertical motion for this area.

On the other hand, the agreement between GPS and PSI data is lower for station MOIT, whose GPS vertical rate through mid 2011 is −31.2 mm/yr, while the PSI data reveal −55.5 mm/yr in 2003–2010 (Fig. 10b). The discrepancy observed in the yearly rates is in part probably due to dissimilar observation time periods, as this is a recently instrumented site with a short time series; on the other hand, record of MOIT station so far indicates a strong influence by seasonal components in the N–S and W–E directions (Fig. 10d), indicating a possible oblique component of the La Colina fault and likely justifying higher residuals (up to 10 mm) between PSI measures and GPS monthly averages. Until a larger instrumentation effort is implemented for all other faults in Morelia, it is still hard to determine whether the observed displacement at MOIT is unique to this fault or if this is a subsidence related widespread behavior that may be observed for other faults. Future studies of land deformation for this area will consequently need to include more sophisticated PSI analyses, possibly exploiting both ascending and descending passes to measure two components of deformation.

4.2. Time-lapse imaged subsidence through InSAR

Our assumption of a linear deformation model for the PSI analysis was driven by the limited temporal sampling of the satellite coverage (averaging about three scenes per year). Points exhibiting strong non linear motion are therefore excluded from the analysis (they do not
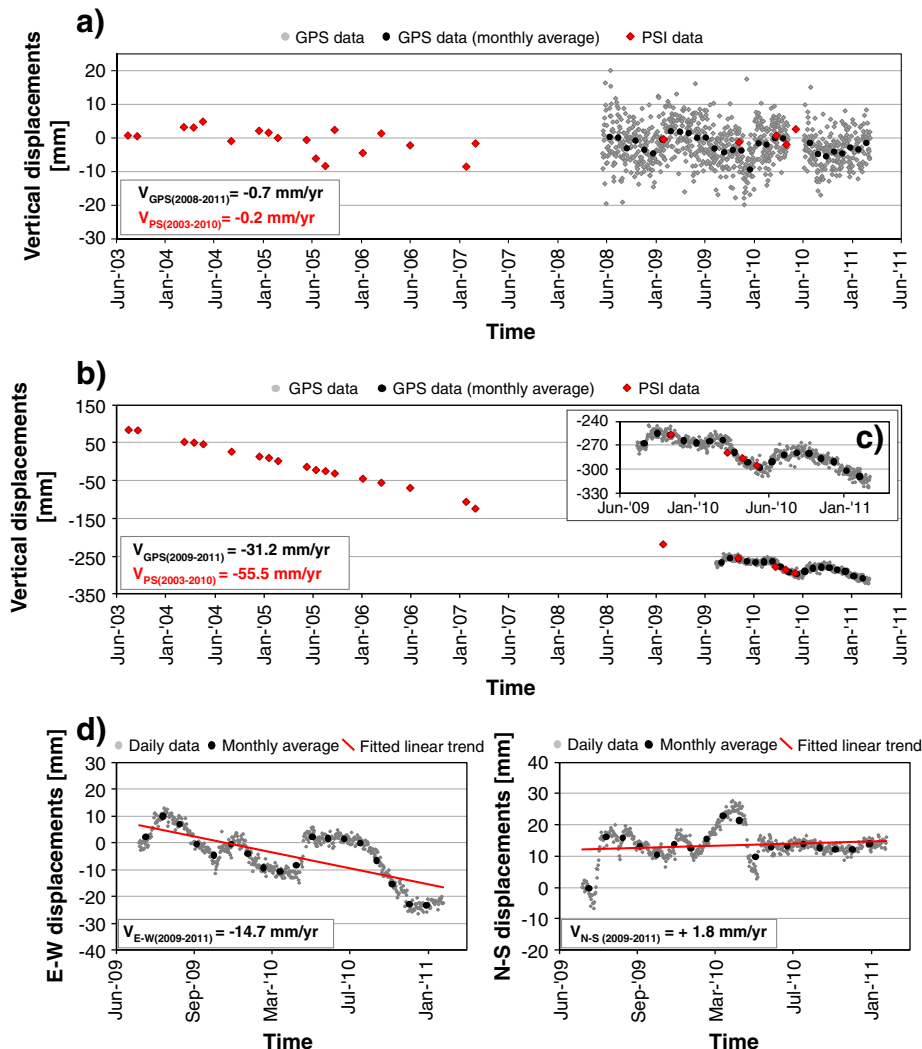

Fig. 10. Vertical displacement time series for GPS sites MOGA (a) and MOIT (b) and their respective representative PS (i.e. closest radar targets to each station). Magnified view (c) of the time series for MOIT station is also represented. E–W and N–S components of the horizontal displacement time series of MOIT are also shown (d).

become PSC or PSP candidates; e.g., Crosetto et al., 2010; Ferretti et al., 2001). To investigate possible time variable deformation in selected areas, we formed differential interferograms and normalized LOS deformation rates for four separate time spans (Fig. 11). For each of the four InSAR pairs, high coherence was observed in the urban area, whereas vegetated areas experienced significant temporal decorrelation between acquisitions.

From the four differential interferograms and their respective displacement rate maps, we make the following observations (Fig. 11):

A) During the July 12th, 2003–November 13th, 2004 period, LOS deformation rates were generally lower than 5–7 mm/yr for most of the urban area. However, displacement rates as high as 25–30 mm/yr (about 3–4 cm in the observed 16 month period) were observed in the area north of La Colina fault, while 10–15 mm/yr (about 1–2 cm) in the sector north of Central Camionera fault and 15–20 mm/yr (about 2–3 cm) south of El Realito fault. A rate of about 10 mm/yr was also observed in a narrow zone north of the La Paloma fault.

B) Between December 18th, 2004 and December 3rd, 2005, displacement rates decreased to about 10–20 mm/yr north of La Colina fault and also south of El Realito fault. In the sector north of Central Camionera fault, a well defined circular area registered LOS deformation rates up to 30–35 mm/yr.

C) Analysis of ground deformations for the period February 11th, 2006 through January 27th, 2007 shows acceleration of ground displacement in all the urban area north of the Central Camionera fault. Subsidence rates reached 25–35 mm/yr north of La Colina fault and 35–50 mm/yr in the circular area north of Central Camionera fault.

D) The December 27th, 2008–October 3rd, 2009 period showed a further acceleration of ground displacements in the area north of Central Camionera fault (up to 75–80 mm/yr; i.e. 6 cm in 10 months), and slightly accelerated rates in the area north of La Colina fault (up to 30–35 mm/yr).

In Fig. 6b, displacement rate profiles relative to the four SAR interferograms are represented along the transect T–T′ (Fig. 1); average deformation rates measured in a 500 m wide buffer zone to the hanging wall and footwall sides of each fault are summarized in Table 3. These profiles confirm the occurrence of differential subsidence as high as 15–35 mm across the main faults (especially prominent on the Central Camionera and La Paloma, and less pronounced for El Realito and Cuautla; Fig. 6b) and uniform deformation within each area, with boundaries defined by major faults.

4.2.1. The Rio Grande meander area

The time-lapse subsidence analysis highlights an interesting pattern of ground subsidence in the meander area of the Rio Grande river, located in the central sector of the city and north of the Central Camionera fault (Fig. 1). A combined map of differential wrapped interferograms and normalized LOS deformation rates for the four InSAR pairs is shown in Fig. 12. An area located between the river and the Central Camionera fault shows 10–15 mm/yr of subsidence in 2003–2004, accelerating to 75–80 mm/yr in 2009. Maximum deformation coincides with the location of the Prados Verdes II (Galeana) water well.

According to OOAPAS archives, this well was rehabilitated in 2001 with 24 h per day service, and with measured static water level and extraction rate of 21 m and 8 l/s, respectively. In 2005, following the installation of a new 8″ casing (the previous one had a 10″ diameter), the length of the pipe increased from 96 to 102 m, and the static level decreased to 22.5 m. Since then, there have been no additional measurements of water extraction rates and static levels; presumably, an increase of the water extraction rates occurred after the 2005 recasing, as well as further depletion of the static level. Assuming a

constant decrease of 0.35 m/yr for this well (calculated with linear interpolation of all the available OOAPAS measurements since 1999), the static level is assumed to be approximately 24.2 m in 2010.

From the observation of the time-lapsed interferograms and deformation maps for the Rio Grande area (Fig. 12), it is evident that recasing this well influenced the subsidence rates of the area, since major displacements are observed beginning in 2005 (pair B; Fig. 12).

The temporal evolution of ground subsidence rates in this area is better illustrated in Fig. 13a, showing a 3D perspective of normalized deformation rates at various times, and the correlation between well location, intense groundwater extraction, and high subsidence.

Profiles of cumulative LOS displacements along cross section P–P′ are shown in Fig. 13b. The slave image of the first InSAR pair (A; 12-Jul-2003) was used as the time reference. Cumulative LOS displacements were then evaluated, progressively adding ground deformations measured through the InSAR analysis in the four time intervals defined in Table 2. In addition to high cumulative deformations near the water extraction location (maximum LOS displacement ~14–15 cm for 2003–2009), a sharp gradient in ground subsidence values occurs across the Central Camionera fault. This step highlights higher subsidence rates in the hanging wall block of this fault, where the thickness of sedimentary deposits and tuffs are much higher than the footwall. Normalized LOS deformation rates and accelerations of LOS displacement measured along the cross section P–P′ are also shown in Fig. 13b. Average acceleration ranges between 10 and 15 mm/yr^2 in 2003–2005 and 2008–2009, while maximum values are observed in 2005–2006, reaching 25 mm/yr^2.

5. Discussion

Since our InSAR- and PSI-based deformation maps show spatial correlations with major faults, we first address the role of tectonics in the observed pattern of subsidence. While the city of Morelia, founded in 1541, has no record of large earthquakes, paleoseismic data (Garduño-Monroy et al., 2009) indicate seismic activity in the mid 1800s near the Morelia region (Singh et al., 1996), suggesting that some of these faults may still be active. Recent shallow geophysical surveys (Cabral-Cano et al., 2010a) carried out across La Colina fault show Neogene displacements of about 8–12 m in the central sector of the fault trace and about 6 m in the eastern sector near the Rio Grande river. Long-term average paleoseismic rates for the La Paloma and La Colina faults are in the range 0.5–0.01 mm/yr respectively (Garduño-Monroy et al., 2009). In contrast, the rates of vertical deformation we observe are up to 7–8 cm/yr, much higher than those normally observed in active tectonic regions.

These observations can be rationalized by a simple model whereby active tectonics related to the Morelia–Acambay fault system (Johnson & Harrison, 1990) controlled overall development of the region and formation of its horst-graben structure, generating a series of small basins with variable thicknesses and compositions of sediments and volcanics. Recent water extraction in these adjacent basins at accelerating rates has resulted in subsidence-induced shallow faulting which mimics pre-existing faults, and in a spatially complex subsidence pattern that exhibits strong fault control, presumably because faults act as impermeable barriers between the various sub-basins, and have also controlled sediment thickness and composition in the various sub-basins. Other studies have documented similar behavior in terms of faults acting as barriers (e.g., Amelung et al., 1999; Hoffmann et al., 2001).

The spatial analysis of land subsidence does not show clear correlation between water well extraction rates and/or static water level drops (Fig. 8). This may reflect the spatial complexity of the system, with a number of small sub-basins with different sediment parameters, and a large number of wells with different depths and pumping rates, and variable proximity to faults.
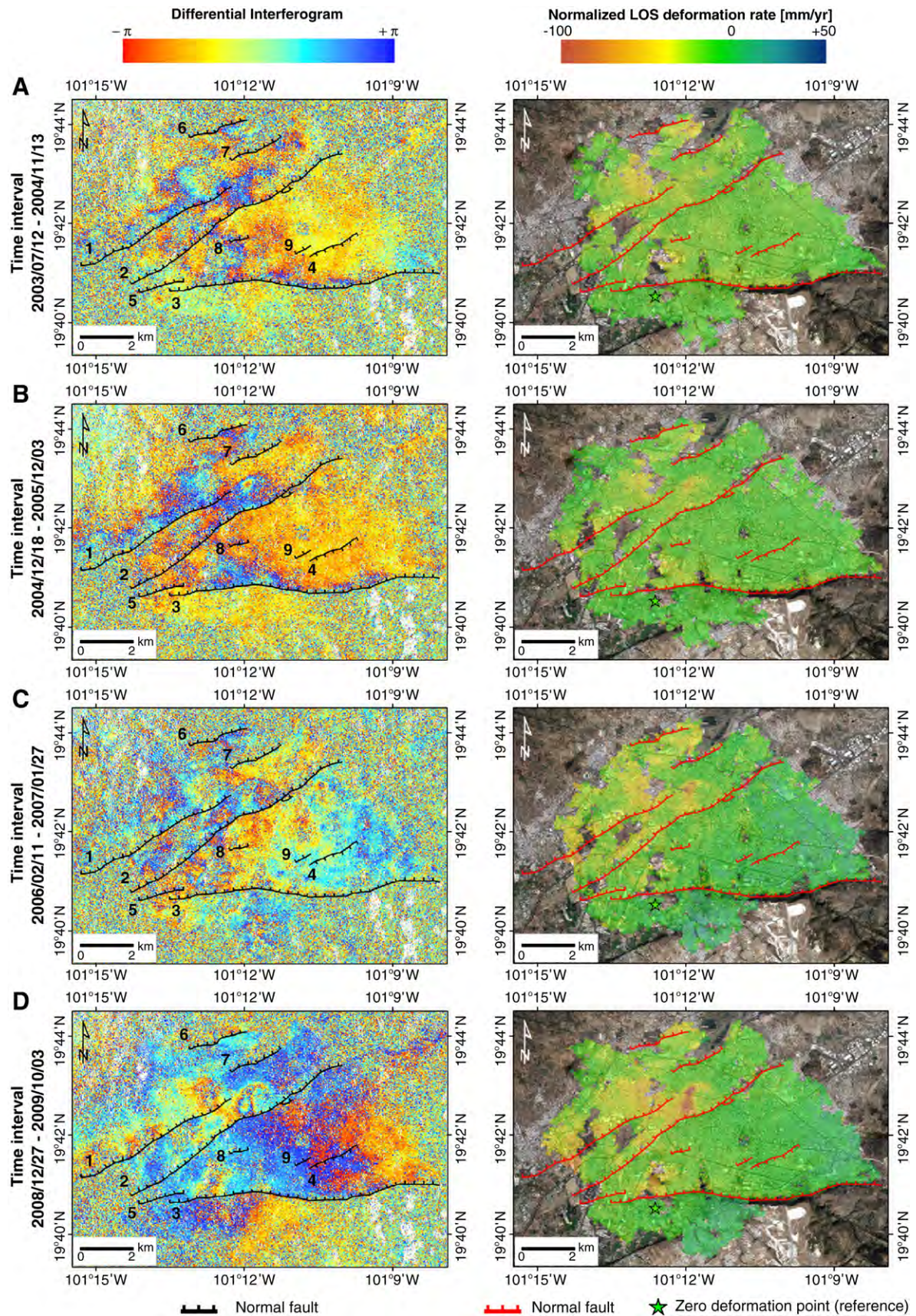
Fig. 11. Temporal evolution of deformation rates in Morelia between 2003 and 2009: ENVISAT differential interferograms (wrapped) and LOS normalized deformation rates for SAR pairs A (12 Jul 2003–13 Nov 2004), B (18 Dec 2004–3 Dec 2005), C (11 Feb 2006–27 Jan 2007) and D (27 Dec 2008–3 Oct 2009), overlaid on Google Earth imagery. Distribution of perpendicular and temporal baselines is summarized in Table 2. Normal faults: 1, La Colina; 2, Central Camionera; 3, La Paloma; 4, Chapultepec; 5, Torremolinos; 6, El Realito; 7, La Soledad; 8, Cuautla; 9, Ventura Puente.
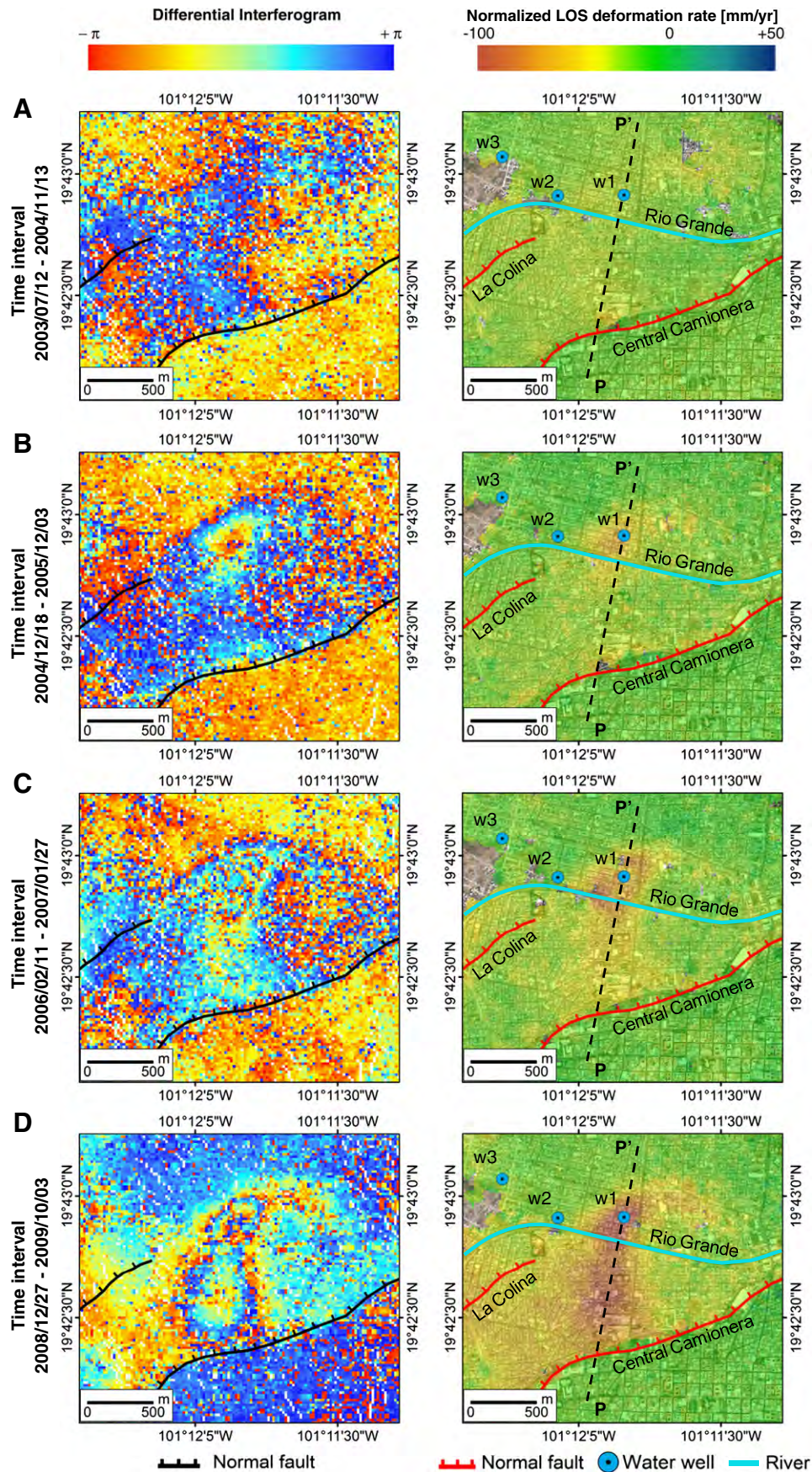
Fig. 12. Temporal evolution of deformation rates for the Rio Grande meander area (Fig. 1) between 2003 and 2009 for the four periods defined in Table 2. The differential interferograms (left side) and LOS normalized deformation rates (right side, based on phase unwrapping) are overlaid on Google Earth imagery. Water wells: w1, Prados Verdes II; w2, Mariano Escobedo II; w3, Mariano Escobedo I. Location of P–P′ cross section is also shown on the deformation maps.
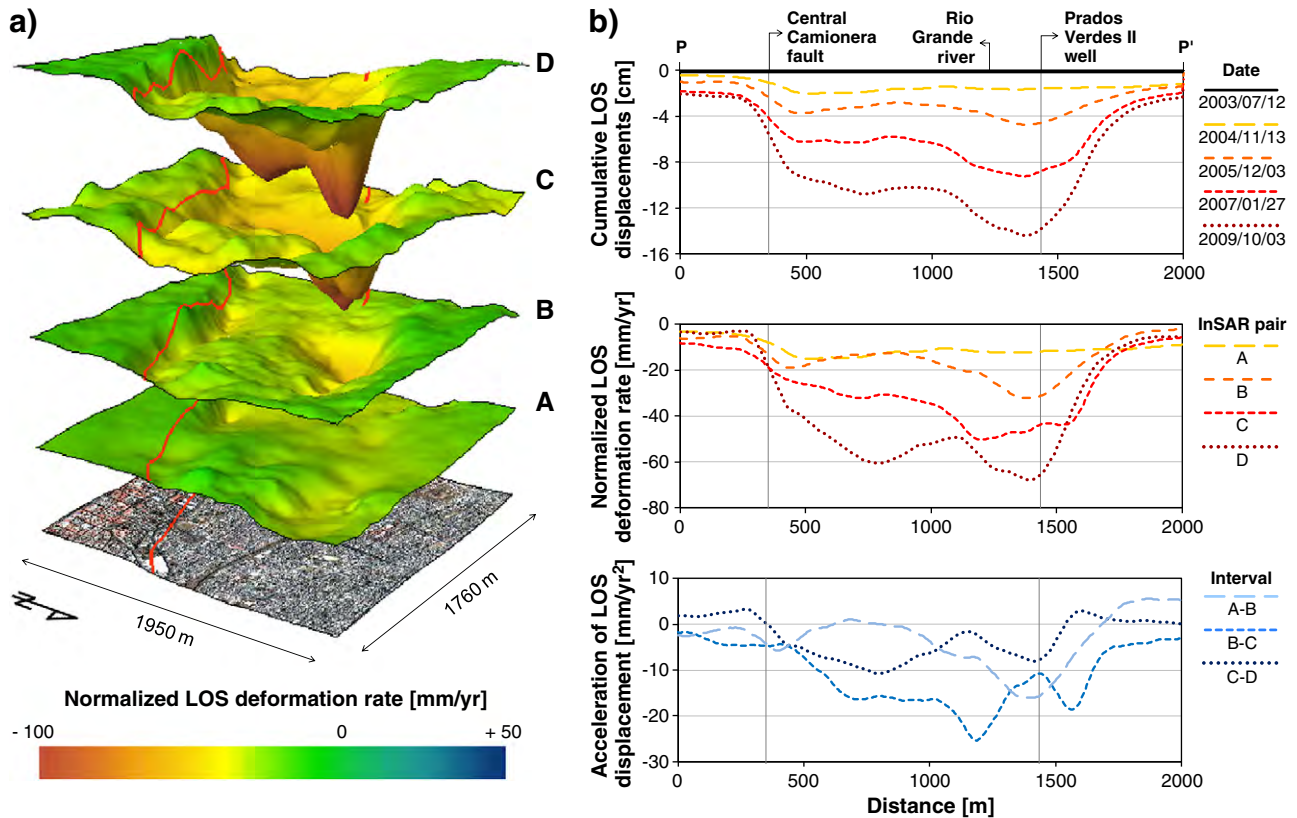
Fig. 13. 2003–2009 InSAR analysis in the Rio Grande meander area: (a) 3D perspective of the temporal evolution of normalized LOS deformation rates; (b) cumulative LOS displacements (displacement rescaled to July 2003), normalized deformation rates and their acceleration, represented along profile P–P′. Location of faults and water wells in the Rio Grande area is shown in Fig. 12, while the time intervals and perpendicular baselines of pairs A, B, C and D are summarized in Table 2.

One exception is the Rio Grande meander area, where intense groundwater withdrawal has led to high subsidence rates (Fig. 12). The spatial characteristics of subsidence in this area, together with the analysis of water well locations, shows a strong correlation between newly observed circular subsidence patterns and intense water pumping from the Prados Verdes II water well, whose location is centered on the peak of ground displacements (maximum LOS displacement of about 14–15 cm in 2003–2010).

Unfortunately current data on pumping rate at this location are not available. Limited available data (8 l/s) are low, but these data are from 2001, prior to the current period of accelerated pumping. Figs. 11 and 13 indicate that subsidence here accelerated after 2005. Additional water extraction data here, in terms of both extraction rates and time series of hydraulic heads, would be extremely useful for assessing the relation between subsidence and local pumping activity.

Two circular areas of intense land deformation, clearly detectable in 2009 (Figs. 12D and 13), suggest the existence of either a local change of the aquifer sediment hydraulic properties inducing a local decrease of subsidence between the two peak areas (e.g., due to prior compaction) or localized shallow groundwater recharge from the Rio Grande river, which would partially counteract the local water table decrease from groundwater extraction. This local component of recharge could explain lower subsidence rates in the middle of cross section P–P′ (1000 m from point P, Figs. 12 and 13b). A more in-depth analysis will need more detailed subsurface data, a comprehensive hydrological characterization and frequent observations of water extraction rates for this area.

Another explanation for the spatial pattern of deformation in this area involves re-activation and possible extension of the La Colina fault, either in the W–E direction (i.e. between the two circular subsidence zones, about 300 m south of the water well and 150 m south of Rio Grande river) or in the SW–NE direction (i.e. 200 m north of the

Prados Verdes II well and tangent to the area with the highest deformation rates; Figs. 12 and 13). However, the observed motion across this potential fault extension is opposite to its expected normal fault behavior, and this hypothesis seems less likely (see Figs. 1 and 11).

Sharp gradients in subsidence are observed across the main faults in Morelia, with significantly higher rates measured on the hanging wall of each one of the faults. One possibility is that differential subsidence is influenced by the contrasting thicknesses of unconsolidated sediments created by post-Miocene tectonics. Compressible deposits and tuffs are much thicker in the hanging wall of the faults; e.g., for the Central Camionera fault, thickness is 120–150 m on the hanging wall, and 30–50 m in the footwall side; for this fault, a sharp increase of about 10 mm/yr, i.e. 7 cm in the 2003–2010 period, can be measured across the fault trace. The compaction rate is also higher for thicker strata of sedimentary material than for thinner strata also for La Colina and La Paloma faults. On the hanging wall of La Colina fault, time-lapse LOS subsidence rates are about 20–30 mm/yr, with some peaks exceeding 40–50 mm/yr (Fig. 6b). A sharp change of 12 mm/yr can be also measured across La Paloma fault (Fig. 6a). The maximum deformation rate of the hanging wall block of La Colina fault as measured by PSI (up to 4–5 cm/yr) is similar to previous estimates from field surveys (4–6 cm/yr; Garduño-Monroy et al., 2001) and a 2005–2007 GPS survey (Ávila-Olivera et al., 2010a).

In the area between La Soledad and La Colina faults, differences in LOS ground deformation (Fig. 6) reflect contrasts in both the thickness and the composition (hydraulic properties) of compressible deposits outcropping near La Colina (Quaternary sedimentary deposits and cemented tuffs) versus basalts and andesites outcropping close to the La Soledad fault.

Faults in Morelia may also act as barriers for horizontal migration of groundwater between the different basins, locally altering the hydraulic response of the aquifer and reducing the permeability of the

sediments across the fault (up to many orders of magnitude less than the surrounding sediments; Antonellini & Aydin, 1994; Forster & Evans, 1991; Haneberg et al., 1999). This is suggested by the sharp contrast of the ground deformation patterns across the Central Camionera in the Rio Grande meander area (Figs. 12 and 13) and also across major faults (Figs. 11 and 2).

Strong differential subsidence in some parts of Morelia may induce a change of the local stress conditions in the fault zones in the future, promoting re-activation of shallow faulting, and is cause for concern. However, for most of the city, subsidence rates in the 2003–2010 study period do not show the extreme values observed in other Mexican cities that experience this phenomenon (e.g., Cabral-Cano et al., 2010b; Osmanoglu et al., 2011). Hence, better urban planning and water management for Morelia could greatly reduce future subsidence, and lead to a sustainable aquifer exploitation.

6. Conclusions

Satellite observations reveal the spatial and temporal complexity of land subsidence affecting the urban area of Morelia in 2003–2010. Critical subsiding zones, their rates of deformation, and their spatial and temporal distribution, are identified and mapped. Groundwater over-exploitation is the dominant process driving land subsidence in Morelia resulting in subsidence-induced shallow faulting which mimics pre-existing faults, with possibly minor contributions from present-day tectonics. The major role of tectonics was to define the geometry of various sub-basins that control aquifer geometry and hydraulic properties. Subsiding areas in Morelia are distributed as either concentrated circular patterns corresponding to locations of intense groundwater extraction (e.g., Rio Grande meander area; maximum deformation of 7–8 cm/yr) or, alternatively, as elongated patterns oriented along NE–SW or E–W directions and parallel to major faults (i.e. La Colina, La Paloma and Central Camionera; maximum deformation of 4–5 cm/yr). High subsidence rates are observed on the hanging wall of major faults, where the thickest sequences of compressible Quaternary sediments crop out. For the Central Camionera fault, an average difference of 1 cm/yr (7–8 cm in the 2003–2010 period) is measured between the hanging wall and footwall. Faults in Morelia may act as barriers to horizontal migration of groundwater. Since ground deformation rates are still modest for most of the urban area, improved urban planning and water management could reduce or eliminate subsidence, preserving productivity of the various aquifers.

Acknowledgments

References

Altamimi, Z., Collilieux, X., Legrand, J., Garayt, B., & Boucher, C. (2007). ITRF2005: A new release of the International Terrestrial Reference Frame based on time series of station positions and Earth Orientation Parameters. *Journal of Geophysical Research*, *112*, B09401, doi:10.1029/2007JB004949.

Amelung, F., Galloway, D. L., Bell, J. W., Zebker, H. A., & Laczniak, R. J. (1999). Sensing the ups and downs of Las Vegas: InSAR reveals structural control of land subsidence and aquifer system deformation. *Geology*, *27*(6), 483–486.

Antonellini, M., & Aydin, A. (1994). Effect of faulting on fluid flow in porous sandstones: Petrophysical properties. *American Association of Petroleum Geologists Bulletin*, *78*, 355–377.

Ávila-Olivera, J. A., & Garduño-Monroy, V. H. (2004). La subsidencia y las fallas geológicas en la ciudad de Morelia, Michoacán. *Proc. XXII Reunión Nacional de Mecánica de Suelos. Guadalajara, Jalisco, México, 18–20 November 2004* (pp. 259–266).

Ávila-Olivera, J. A., & Garduño-Monroy, V. H. (2006). Hundimientos ocasionados por Procesos de Subsidencia-Creep-Falla (PSCF) en la Ciudad de Morelia, Mich. México. *Geotermia, Revista Mexicana de Geoenergía*, *19*(2), 50–59.

Ávila-Olivera, J. A., & Garduño-Monroy, V. H. (2008). A GPR study of subsidence-creep-fault processes in Morelia, Michoacán, Mexico. *The Engineering Geologist*, *100*(1–2), 69–81.

Ávila-Olivera, J. A., & Garduño-Monroy, V. H. (2010). Conceptual model of land subsidence with a structural control. In D. Carreón-Freyre (Ed.), *Land subsidence, associated hazards and the role of natural resources development. Hydrological Sciences Journal, Red Book Series*. (pp. 195–197) Wallingford, Oxfordshire: IAHS Press IAHS Publ. n. 339.

Ávila-Olivera, J. A., Farina, P., & Garduño-Monroy, V. H. (2008). Integration of InSAR and GIS in the study of superficial faults caused by Subsidence-Creep-Fault Proceses in Celaya, Guanajuato. *AIP Conference Proceedings, GIS in Geology and Earth Sciences: 4th International Conference: In Vista of New Approaches for the Geoinformatics, Vol. 1009, No. 1*. (pp. 200–211).

Ávila-Olivera, J. A., Farina, P., & Garduño-Monroy, V. H. (2010). Land subsidence monitored by satellite interferometry in Mexican cities. In D. Carreón-Freyre (Ed.), *Land subsidence, associated hazards and the role of natural resources development. Hydrological Sciences Journal, Red Book Series*. (pp. 316–318) Wallingford, Oxfordshire: IAHS Press IAHS Publ. n. 339.

Ávila-Olivera, J. A., Garduño-Monroy, V. H., & Farina, P. (2010). Integrated study of land subsidence in Morelia, Michoacán, Mexico. In D. Carreón-Freyre (Ed.), *Land subsidence, associated hazards and the role of natural resources development. Hydrological Sciences Journal, Red Book Series*. (pp. 185–190) Wallingford, Oxfordshire: IAHS Press IAHS Publ. n. 339.

Bawden, G. W., Thatcher, W., Stein, R. S., Hudnut, K. W., & Peltzer, G. (2001). Tectonic contraction across Los Angeles after removal of groundwater pumping effects. *Nature*, *412*, 812–815.

Bürgmann, R., Hilley, G. E., & Ferretti, A. (2006). Resolving vertical tectonics in the San Francisco Bay Area from Permanent Scatterer InSAR and GPS Analysis. *Geology*, *34*, 221–224.

Cabral-Cano, E., Arciniega-Ceballos, A., Díaz-Molina, O., Cigna, F., Osmanoglu, B., Dixon, T., DeMets, C., Vergara-Huerta, F., Garduño-Monroy, V. H., Ávila-Olivera, J. A., & Hernández-Quintero, E. (2010). Is there a tectonic component on the subsidence process in Morelia, Mexico? In D. Carreón-Freyre (Ed.), *Land subsidence, associated hazards and the role of natural resources development. Hydrological Sciences Journal, Red Book Series*. (pp. 164–169) Wallingford, Oxfordshire: IAHS Press IAHS Publ. n. 339.

Cabral-Cano, E., Dixon, T. H., Miralles-Wilhelm, F., Díaz-Molina, O., Sánchez-Zamora, O., & Carande, R. E. (2008). Space geodetic imaging of rapid ground subsidence in Mexico City. *Geological Society of America Bulletin*, *120*(11–12), 1556–1566.

Cabral-Cano, E., Osmanoglu, B., Dixon, T., Wdowinski, S., DeMets, C., Cigna, F., & Díaz-Molina, O. (2010). Subsidence and fault hazard maps using PSInSAR and permanent GPS networks in central Mexico. In D. Carreón-Freyre (Ed.), *Land subsidence, associated hazards and the role of natural resources development. Hydrological Sciences Journal, Red Book Series*. (pp. 255–259) Wallingford, Oxfordshire: IAHS Press IAHS Publ. n. 339.

Carrillo, N. (1948). Influence of artesian wells on the sinking of México City. *Proc. 2nd Int. Conference on Soils Mechanics: Rotterdam, Holland. International Society for Soil Mechanics and Geotechnical Engineering, vol. VII.*

Chen, C. W., & Zebker, H. A. (2000). Network approaches to two-dimensional phase unwrapping: Intractability and two new algorithms. *Journal of the Optical Society of America. A*, *17*, 401–414.

Crosetto, M., Monserrat, O., Iglesias, R., & Crippa, B. (2010). Persistent Scatterer Interferometry: Potential, limits and initial C- and X-band comparison. *Photogrammetric Engineering and Remote Sensing*, *76*(9), 1061–1069.

Dixon, T. H., Amelung, F., Ferretti, A., Novali, F., Rocca, F., Dokka, R., Sella, G., Kim, S. W., Wdowinski, S., & Whitman, D. (2006). Subsidence and flooding in New Orleans — A subsidence map of the city offers insight into the failure of the levees during Hurricane Katrina. *Nature*, *441*, 587–588.

Farina, P., Ávila-Olivera, J. A., & Garduño-Monroy, V. H. (2007). Structurally-controlled Urban Subsidence along the Mexican Volcanic Belt (MVB) monitored by InSAR. *Proc. Envisat Symposium 2007. Montreux, Switzerland, 23–27 April 2007.* : ESA CD-ROM.

Farina, P., Ávila-Olivera, J. A., Garduño-Monroy, V. H., & Catani, F. (2008). DInSAR analysis of differential ground subsidence affecting urban areas along the Mexican Volcanic Belt (MVB). *Rivista Italiana di Telerilevamento (AIT), Il Telerilevamento a microonde, L'attività di ricerca e le applicazioni*, *40 (2)*. (pp. 103–113).

Ferretti, A., Prati, C., & Rocca, F. (2001). Permanent Scatterers in SAR interferometry. *IEEE Transactions on Geoscience and Remote Sensing*, *39*(1), 8–20.

Forster, C. B., & Evans, J. P. (1991). Hydrogeology of thrust faults and crystalline thrust sheets: Results of combined field and modeling studies. *Geophysical Research Letters*, *18*, 979–982.

Galloway, D. L., Hudnut, K. W., Ingebritsen, S. E., Phillips, S. P., Peltzer, G., Rogez, F., & Rosen, P. A. (1998). Detection of aquifer system compaction and land subsidence using interferometric synthetic aperture radar, Antelope Valley, Mojave Desert, California. *Water Resources Research*, *34*(10), 2573–2585.

Garduño-Monroy, V. H., Pérez-Lopez, R., Israde-Alcantara, I., Rodríguez-Pascua, M. A., Szynkaruk, E., Hernández-Madrigal, V. M., García-Zepeda, M. L., Corona-Chávez, P., Ostroumov, M., Medina-Vega, V. H., García-Estrada, G., Carranza, O., Lopez-Granados, E., & Mora Chaparro, J. C. (2009). Paleoseismology of the southwestern Morelia–Acambay fault system, central México. *Geofísica Internacional*, *48*(3), 319–335.

Garduño-Monroy, V. H., Arreygue-Rocha, E., Chiesa, S., Israde-Alcántara, I., Rodríguez-Torres, G. M., & Ayala, G. M. (1998). Las fallas geológicas y sísmicas de la Ciudad de Morelia y su influencia en la planificación del territorio. *Ingeniería Civil*, *1*(5), 3–12.

Garduño-Monroy, V. H., Arreygue-Rocha, E., Israde-Alcántara, I., & Rodríguez-Torres, G.M. (2001). Efectos de las fallas asociadas a sobreexplotación de acuíferos y la presencia de fallas potencialmente sísmicas en Morelia, Michoacán, México. *Revista Mexicana de Ciencias Geológicas*, *18*(1), 37–54.

Garduño-Monroy, V. H., Rodríguez-Torres, G. M., Israde-Alcántara, I., Arreygue-Rocha, E., Canuti, P., & Chiesa, S. (1999). Efectos del clima (El Niño) en los fenómenos de fluencia de las fallas geológicas de la ciudad de Morelia. *Geos, Unión Geofísica Mexicana*, *9*(2), 84–93.

Gayol, R. (1925). Estudio de las perturbaciones que en el fondo de la Ciudad de México ha producido el drenaje de las aguas del subsuelo, por las obras del desague y rectificación de los errores a que ha dado lugar una incorrecta interpretación de los efectos producidos. *Revista Mexicana de Ingeniería y Arquitectura*, *III*. (pp. 96–132).

Goldstein, R. M., & Werner, C. L. (1998). Radar interferogram filtering for geophysical applications. *Geophysical Research Letters*, *25*(21), 4035–4038.

Goldstein, R. M., Engelhardt, H., Kamb, B., & Frolich, R. M. (1993). Satellite radar interferometry for monitoring ice sheet motion: Application to an Antarctic ice stream. *Science*, *262*(5139), 1525–1530.

Haneberg, W. C., Mozley, P. S., Moore, J. C., & Goodwin, L. B. (1999). Faults and subsurface fluid flow in the shallow crust. *American Geophysical Union, Geophysical Monographs*, *113*, 7–26.

Hanssen, R. F. (2005). Satellite radar interferometry for deformation monitoring: A priori assessment of feasibility and accuracy. *International Journal of Applied Earth Observation and Geoinformation*, *6*, 253–260.

Herrera, G., Fernandez, J. A., Tomas, R., Cooksley, G., & Mulas, J. (2009). Advanced interpretation of subsidence in Murcia (SE Spain) using A-DInSAR data—Modelling and validation. *Natural Hazards Earth System Sciences*, *9*, 647–661.

Hilley, G. E., Burgmann, R., Ferretti, A., Novali, F., & Rocca, F. (2004). Dynamics of slow-moving landslides from Permanent Scatterer analysis. *Science*, *304*(5679), 1952–1955.

Hoffmann, J., Zebker, H. A., Galloway, D. L., & Amelung, F. (2001). Seasonal subsidence and rebound in Las Vegas Valley, Nevada, observed by synthetic aperture radar interferometry. *Water Resources Research*, *37*(6), 1551–1566.

Hooper, A., Zebker, H., Segall, P., & Kampes, B. (2004). A new method for measuring deformation on volcanoes and other natural terrains using InSAR persistent scatterers. *Geophysical Research Letters*, *31*(23), L23611, doi:10.1029/2004GL021737.

Johnson, C. A., & Harrison, C. G. A. (1990). Neotectonics in central México. *Physics of the Earth and Planetary Interiors*, *64*(2–4), 187–210.

Kampes, B., & Usai, S. (1999). Doris: The delft object-oriented radar interferometric software. *Proc. 2nd Int. Symp. Operationalization of Remote Sensing*. Enschede, The Netherlands: ITC.

Ketelaar, V. B. H. (2009). *Satellite radar interferometry: Subsidence monitoring techniques.* New York: Springer Verlag (Chapter 3).

Kim, S. -W., Wdowinski, S., Amelung, F., Dixon, T. H., Won, S. -J., & Kim, J. -W. (2010). Measurements and predictions of subsidence induced by soil consolidation using permanent scatterer InSAR and hyperbolic model. *Geophysical Research Letters*, *37*, L05304, doi:10.1029/2009GL041644.

Kimura, H., & Yamaguchi, Y. (2000). Detection of landslide areas using satellite radar interferometry. *Photogrammetric Engineering and Remote Sensing*, *66*(3), 337–344.

Lermo-Samaniego, J., Nieto-Obregón, J., & Zermeño, M. (1996). Fault and fractures in the valley of Aguascalientes. Preliminary microzonification. *World Conference on Earthquake Engineering, 11th Amsterdam, Elsevier, Paper n. 1651*.

López-Quiroz, P., Doin, M. P., Tupin, F., Briole, P., & Nicolas, J. M. (2009). Time series analysis of Mexico City subsidence constrained by radar Interferometry. *Journal of Applied Geophysics*, *69*(1), 1–15.

Martínez-Reyes, J., & Nieto-Samaniego, A. F. (1990). Efectos geológicos de la tectónica reciente en la parte central de México. *Revista mexicana de ciencias geológicas*, *9* (1), 33–50.

Massonnet, D., & Feigl, K. L. (1998). Radar interferometry and its application to changes in the Earth's surface. *Reviews of Geophysics*, *36*, 441–500.

Massonnet, D., Briole, P., & Arnaud, A. (1995). New insights on Mount Etna from 18 months of radar interferometric monitoring. *Nature*, *375*, 567–570.

Ortega-Guerrero, A., Cherry, J. A., & Rudolph, D. L. (1993). Large-Scale aquitard consolidation near Mexico City. *Groundwater*, *31*(5), 708–718.

Osmanoglu, B. (2010). http://code.google.com/p/adore-doris/ accessed on September 7th, 2011

Osmanoglu, B., Dixon, T. H., Wdowinski, S., Cabral-Cano, E., & Jiang, Y. (2011). Mexico City subsidence observed with persistent scatterer InSAR. *International Journal of Applied Earth Observation and Geoinformation*, *13*(1), 1–12.

Rosen, P. A., Hensley, S., Joughin, I. R., Li, F. K., Madsen, S. N., Rodriguez, E., & Goldstein, R. M. (2000). Synthetic aperture radar interferometry. *Proc. IEEE, 88 (3.* (pp. 333–382).

Scharroo, R., & Visser, P. (1998). Precise orbit determination and gravity field improvement for the ERS satellites. *Journal of Geophysical Research*, *103*(C4), 8113–8127.

Singh, S. K., Ordaz, M., & Pérez-Rocha, L. (1996). The great Mexican earthquake of 19 June 1858: Expected ground motion and damage in México City from a similar future event. *Bulletin of the Seismological Society of America*, *86*(6), 1655–1666.

Singhroy, V., Mattar, K., & Gray, L. (1998). Landslide characterization in Canada using interferometric SAR and combined SAR and TM images. *Advances in Space Research*, *2*, 465–476.

Sousa, J. J., Ruiz, A. M., Hanssen, R. F., Bastos, L., Gil, A. J., Galindo-Zaldívar, J., & Sanz de Galdeano, C. (2010). PS-InSAR processing methodologies in the detection of field surface deformation—Study of the Granada basin (Central Betic Cordilleras, southern Spain). *Journal of Geodynamics*, *49*(3–4), 181–189.

Strozzi, T., & Wegmüller, U. (1999). Land subsidence in Mexico City mapped by ERS differential SAR Interferometry. *Proc. IGARSS 1999, 19th IEEE International Geoscience and Remote Sensing Symposium, Hamburg, Germany, 4.* (pp. 1940–1942).

Strozzi, T., Wegmuller, U., Werner, C., & Wiesmann, A. (2002). JERS SAR Interferometry for land subsidence monitoring. In A. Wilson, & S. Quegan (Eds.), *Proc. Third International Symposium on Retrieval of Bio- and Geophysical Parameters from SAR Data for Land Applications. ESA Publication, vol. 475.* (pp. 145–150).

Tomás, R., Márquez, Y., Lopez-Sanchez, J. M., Delgado, J., Blanco, P., Mallorquí, J. J., Martínez, M., Herrera, G., & Mulas, J. (2005). Mapping ground subsidence induced by aquifer overexploitation using advanced Differential SAR Interferometry: Vega Media of the Segura River (SE Spain) case study. *Remote Sensing of Environment*, *98*(2–3), 269–283.

Trejo-Moedano, A., & Martinez-Baini, A. (1991). Agrietamientos de suelos en la zona de Querétaro. *Agrietamientos de Suelos. Sociedad Mexicana de Mecánica de Suelos, México* (pp. 67–74).

Trujillo-Candelaria, J. A. (1985). Subsidencia de terrenos en la ciudad de Celaya, Gto. *Reunión sobre Asentamientos Regionales: México, D.F., Sociedad Mexicana de Suelos, Asociación Geohidrólogica Mexicana* (pp. 1–2).

Webb, F. H., & Zumberge, J. F. (1997). An introduction to GIPSY/OASIS-II. *Technical Report JPL D-11088*. Pasadena, CA: Jet Propulsion Lab.

Werner, C., Wegmüller, U., Strozzi, T., & Wiesmann, A. (2000). Gamma SAR and interferometric processing software. *Proc. ERS-ENVISAT Symposium, Gothenburg, Sweden, 16–20 October 2000.*

Werner, C., Wegmüller, U., Strozzi, T., & Wiesmann, A. (2003). Interferometric Point Target Analysis for deformation mapping. *Proc. IGARSS 2003, 23rd IEEE International Geoscience and Remote Sensing Symposium, Toulouse, France, 21–25 July 2003* (pp. 4362–4364).

Willis, P., Jayles, C., & Bar-Sever, Y. (2006). DORIS: From orbit determination for altimeter missions to geodesy. *Comptes Rendus Geosciences*, *338*(14–15), 968–979.